

The Method of Total Scattering and Atomic Pair Distribution Function Analysis

Chapter Outline

3.1. Total Scattering and the PDF	56	3.4. The PDF in Higher Dimensions	89
3.1.1. Introduction	56	3.4.1. PDF Defined in Three Dimensions	89
3.1.2. The PDF as the Fourier Transform of the Scattered Intensity	57	3.4.2. Anisotropic PDF	90
3.1.3. The PDF and All Its Friends and Relations	69	3.4.3. One-Dimensional PDF and Layer–Layer Correlations	91
3.1.4. Brief History	73	3.4.4. Two-Dimensional PDF and Intralayer Correlation	92
3.1.5. Multicomponent Systems	77	3.4.5. Three-Dimensional PDF and the Powder PDF	95
3.2. Compositionally Resolved Partial PDF	80	3.5. Error Analysis for the PDF	95
3.2.1. Differential PDF	80	3.5.1. Error Diagnostics	95
3.2.2. Anomalous X-Ray Scattering	81	3.5.2. Termination and Normalization Errors	96
3.2.3. Isotopic Substitution	83	3.5.3. Statistical Errors	97
3.2.4. Joint Total and Differential PDF Studies	86	3.5.4. Effect of Q -Resolution	98
3.3. Magnetic Correlation Functions	86	3.5.5. Effect of Other Systematic Errors	99
3.3.1. Magnetic Scattering of Neutrons	86	3.5.6. Remedies of Errors	100
3.3.2. Magnetic PDF	87		

3.6. Information Content in the PDF and the Nyquist–Shannon Sampling Theorem	100	Appendix 3.3 The X-Ray Absorption Fine Structure Method	106
Appendix 3.1 Beevers–Lipson Strips	103	Appendix 3.4 Anisotropic PDF Method	108
Appendix 3.2 Termination Error	105		

3.1. TOTAL SCATTERING AND THE PDF

3.1.1. Introduction

As we discussed in Chapter 2, in standard crystallographic analysis, the Bragg peaks and diffuse-scattering intensities were treated separately. The structure is determined solely based upon the information provided by the position and intensity of the Bragg peaks, while additional information regarding deviations from the perfect lattice is obtained through the study of diffuse scattering. This approach makes sense when the deviations are small, but when the structure is extensively disordered it fails in practice.

In this chapter, we present an alternative approach which treats both the Bragg and the diffuse scattering on an equal basis, the so-called total-scattering technique. Data from throughout reciprocal space, over a wide range of Q values, are utilized. The technique is both straightforward and intuitively easy to comprehend. A convenient tool here is the Fourier transformation. In analyzing a complex function, Fourier analysis quite often provides distinct and useful information that is easier to interpret. For instance, a computer distinguishes human voices more readily in their Fourier transforms and holographic radar also uses Fourier analysis as the principle of the method. In the case of diffraction, it is even more compelling to consider the Fourier transformation since it has a very well defined physical meaning. Fourier analysis of the total-scattering data is known as atomic pair distribution function (PDF) analysis.

We first introduce the basic ideas and equations of total scattering and PDF analysis and give a brief and incomplete history of the subject. From [Section 3.2](#) onward, we explore in more detail the application of the technique to different specialized situations such as obtaining compositionally resolved information, magnetic short-range order, and studying samples in special geometries. These sections can be omitted on a first reading without affecting the reader's ability to understand later chapters. Finally, we discuss errors of the PDF, with respect to their origin and methods to minimize them. This is an important section, as the accuracy of the PDF method is often underestimated, and given as an excuse to avoid this powerful technique. This subject is discussed also in [Appendix 5.3](#) in further detail.

3.1.2. The PDF as the Fourier Transform of the Scattered Intensity

The basis of the total-scattering method is the normalized, measured, scattering intensity from a sample, the total-scattering structure function, $S(\mathbf{Q})$. This intensity distribution is a continuous function of the wavevector, \mathbf{Q} , and, in general, contains both Bragg and diffuse intensity. It is the theoretical normalized scattering intensity from the atoms in a material, and formally derived in Chapter 2, and below.

We begin by restating Eq. (2.4), the scattering amplitude

$$\Psi(\mathbf{Q}) = \frac{1}{\langle b \rangle} \sum_v b_v e^{i\mathbf{Q} \cdot \mathbf{R}_v}. \quad (3.1)$$

In Eq. (3.1), \mathbf{R}_v defines the position of the v th atom, b_v is the scattering amplitude of the atom v , that is, a measure of how strongly it scatters, and $\langle \cdots \rangle$ represents a compositional average,

$$\langle b \rangle = \frac{1}{N} \sum_v b_v = \sum_\alpha c_\alpha b_\alpha. \quad (3.2)$$

Here, the sum over v is over every atom in the sample. In practice, this is more conveniently expressed as a sum, α , over atomic species where c_α is the atomic fraction and b_α is the scattering amplitude of the element α , as indicated in Eq. (3.2).

We get the scattered intensity, and the scattering cross sections introduced in Chapter 2, by taking the modulus squared of Eq. (3.1),

$$\begin{aligned} \frac{d\sigma_C(\mathbf{Q})}{d\Omega} &= \frac{\langle b \rangle^2}{N} |\Psi(\mathbf{Q})|^2 = \frac{1}{N} \sum_{v,\mu} b_v b_\mu e^{i\mathbf{Q} \cdot (\mathbf{R}_v - \mathbf{R}_\mu)}, \\ I(\mathbf{Q}) &= \frac{d\sigma_C(\mathbf{Q})}{d\Omega} \langle b \rangle^2 - \langle b^2 \rangle, \\ S(\mathbf{Q}) &= \frac{I(\mathbf{Q})}{\langle b \rangle^2}. \end{aligned} \quad (3.3)$$

This serves to define $S(\mathbf{Q})$, the function known as the total-scattering structure function, or often just structure function, which converges to unity at large Q . In the liquid and glass community, $S(\mathbf{Q})$, an intensity, is usually, and confusingly, called the structure factor. In the crystallographic community, the term structure factor scales the amplitude, $\Psi(\mathbf{Q})$, (Eq. 3.1). The crystallographic structure factor is defined in Eq. (2.14). Also, in the inelastic scattering community, $S(\mathbf{Q}, \omega)$, discussed in Chapter 7, is called the dynamic structure factor.

The conflicting naming in different communities has been a source of much confusion. In order to avoid such confusion in this book, we use the term sample scattering amplitude to define $\Psi(\mathbf{Q})$ and call $S(\mathbf{Q})$ the structure function. The term $\langle b \rangle^2 - \langle b \rangle$ in the expression for $S(\mathbf{Q})$ is called the Laue monotonic scattering and is needed for convenience simply because $d\sigma_c/d\Omega$ approaches $\langle b^2 \rangle$ at large Q , while we want to make $S(\mathbf{Q})$ approach unity at large Q . Actually, it is possible to define $S(\mathbf{Q})$ differently by normalizing with respect to $\langle b^2 \rangle$ rather than $\langle b \rangle^2$. In many situations, the scattering is isotropic; it depends only on the magnitude of the wavevector, Q , but not its direction. This is true of scattering from microscopically isotropic samples such as gases, liquids, and glasses. It is also true from samples of finely powdered crystallites. Each crystallite is not isotropic, but scattering from the ensemble is isotropic. Later in the chapter, we will discuss extensions to cases where the scattering is not isotropic. However, the greatest utility of the technique to date has been to study the isotropic scattering from powdered crystallites, liquid, or glassy samples. We therefore consider the subject in this straightforward limit first. Examples of some $S(Q)$ functions (expressed as the reduced structure function, $F(Q) = Q[S(Q) - 1]$) from exemplar crystalline and amorphous materials are shown in Fig. 3.1.

As we discussed in Section 2.1.2, in the kinematical scattering theory, the microscopic real-space density of a material is simply given by a Fourier transform of the scattering amplitude, $\Psi(Q)$. Similarly, the Fourier transform of the scattered *intensity*, in the form of the structure function $S(Q)$, yields the atomic pair distribution function, $g(r)$. For many years, including as Eq. (3.1) in the first edition of this book, we have been slightly lazily writing the expression for the reduced pair distribution function, $G(r)$, as

$$G(r) = \left(\frac{2}{\pi}\right) \int_0^\infty F(Q) \sin(Qr) dQ, \quad (3.4)$$

where $F(Q)$ is the reduced structure function, $F(Q) = Q[S(Q) - 1]$, and

$$G(r) = 4\pi r[\rho(r) - \rho_0] = 4\pi r\rho_0[g(r) - 1]. \quad (3.5)$$

Here, $\rho(r)$ is the atom-pair density function more formally derived below, $g(r)$ is called the pair distribution function, and ρ_0 is the atomic number density. We have been lazy writing this equation because we neglect the asymptotic behavior of the function at the limits $Q \rightarrow 0$ and $Q \rightarrow \infty$, merely mentioning that in real experiments, we cannot reach zero or infinity in Q and so from a practical perspective the right equation is actually

$$G(r) = \left(\frac{2}{\pi}\right) \int_{Q_{\min}}^{Q_{\max}} F(Q) \sin(Qr) dQ, \quad (3.6)$$

where experimental limitations determine the values of Q_{\min} and Q_{\max} . In fact, a recent rederivation of the PDF equations, carried out in a way to make explicit their relationship to the small-angle scattering equations (Farrow and Billinge, 2009),

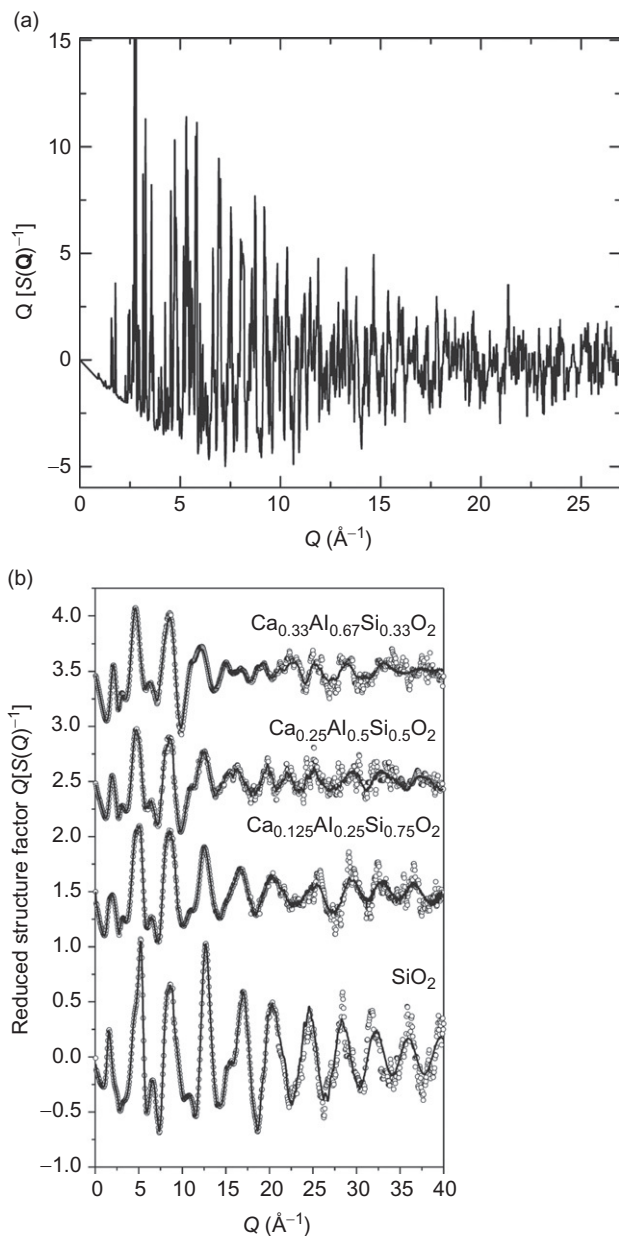


FIGURE 3.1 Exemplar total-scattering structure functions, $S(Q)$ (plotted as $Q(S(Q) - 1)$), for representative crystalline and amorphous materials: (a) crystalline LaMnO_3 powder at $T = 10$ K (Proffen *et al.*, 1999); (b) amorphous aluminosilicates (Petkov *et al.*, 2000b). Note the sharp features in the crystalline $S(Q)$ compared with the broad diffuse scattering from the amorphous materials.

shows that Eq. (3.4) is actually *strictly incorrect* from theoretical considerations, not just from experimental ones, the correct equation being

$$\frac{R(r)}{r} = \left(\frac{2}{\pi}\right) \int_0^\infty F(Q) \sin(Qr) dQ, \quad (3.7)$$

where $R(r)$ is the radial distribution function (RDF), described below. When you include the small-angle scattering in the Fourier transform, you do not get $G(r)$, you get $R(r)/r$. On the other hand, in most practical cases (strictly, when the small-angle scattering is all below Q_{\min} and therefore excluded but all the wide-angle diffraction is above Q_{\min}), Eq. (3.6) is actually correct, and for most practical purposes, this is the experimentally accessed equation, though as we discuss later in this book, there is currently a trend toward combining small-angle and wide-angle data in the analysis of materials, in which case this distinction becomes important.

Historically, this distinction had little bearing on anything as bulk materials such as liquids, amorphous materials, and crystalline materials were being studied and they had no small-angle scattering, or rather the small-angle scattering was in the forward-scattering direction and not distinguishable from the direct beam. This changes when nanomaterials such as nanoparticles and nanoporous materials are being studied. In this case, there may be considerable small-angle scattering coming from the finite size of the scattering objects. In fact, when the scattering objects are very small, less than 10 nm, for example, the small-angle scattering appears at quite accessible values of Q . As we discuss in Chapter 4, a number of instruments and experiments are now explicitly capturing this small-angle information to complement the wide-angle PDF data.

As described in Section 1.1.4, $g(r)$ is like a distance map of the inside of the solid. The function gives the probability of finding two atoms separated by the distance, r . An example is shown in Fig. 3.2 (Louca and Egami, 1999).

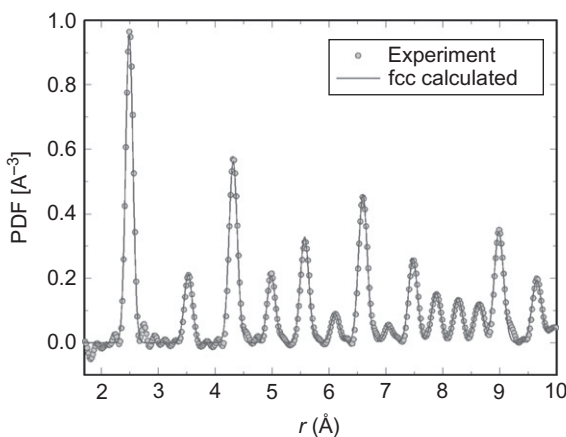


FIGURE 3.2 The PDF of crystalline Ni at $T = 10$ K (Louca and Egami, 1999).

The circles are the measured PDF of nickel obtained by Fourier transforming the measured total-scattering structure function. The solid line is the PDF of the nickel crystal structure calculated using Eq. (1.1). The closest that two atoms can approach each other is the nearest neighbor distance, r_{nn} , which in nickel is 2.50 Å, and corresponds to the first peak. There is no peak in the PDF before this value; small peaks at shorter distances come from noise (both systematic and random). Nickel has the fcc structure with a lattice parameter of $a = 3.54$ Å. Therefore, the nearest neighbor peak is from the unit-cell corner to the face center: $a/\sqrt{2} = 2.50$ Å which appears as expected in the figure. Each of the peaks in the PDF can be attributed to some such atom–atom relationship or atomic–atom correlations. If we have a model for the atomic structure, specified by atomic positions in space, it is trivial to calculate $g(r)$ and compare with experimentally measured correlation functions.

The PDF is related to the Patterson function introduced in Section 2.2.2. Usually, only the Bragg peaks are used in calculating the Patterson function which therefore has the periodicity of the lattice. Both the Bragg peaks and diffuse intensity are included in obtaining the PDF. Thus, the PDF does not necessarily have the lattice periodicity and will be able to describe the deviations from lattice periodicity. One may also say that the PDF defined by Eq. (3.4) is a spherically averaged generalized Patterson function.

The inverse transformation of Eq. (3.4) can be defined, and it yields the structure function $S(Q)$ in terms of $G(r)$,

$$S(Q) = 1 + \frac{1}{Q} \int_0^\infty G(r) \sin(Qr) dr. \quad (3.8)$$

3.1.2.1. Derivation of the PDF Equations

Here, we start from the equation for the scattering amplitude (Eq. 3.1) and derive the PDF equations summarized in Section 3.1.2. This treatment appeared in full in Farrow and Billinge (2009). It follows a long tradition of obtaining these equations going back to the 1920s and the work of Zernicke and Prins (1927), but this treatment makes a bit more explicit the relationship between the PDF equations and those used in the small-angle scattering literature. This turns out to be especially important when we consider PDFs of finite clusters and nanoparticles, one of the emerging focuses of PDF studies, coupled with our emerging ability to obtain small-angle (or rather “medium” angle as opposed to real small angle or wide angle) data routinely at the same time as the PDF data, for example, at the NIMROD or NOMAD instrument and with a number of RAPDF beam line setups.

We start by restating Eq. (3.1), the scattering amplitude for a series of atoms, i ,

$$\begin{aligned} \Psi(\mathbf{Q}) &= \sum_i f_i(Q) \exp(i\mathbf{Q} \cdot \mathbf{r}_i) \\ &= \sum_i \psi_i, \end{aligned} \quad (3.9)$$

which defines ψ_i . The sum is over all the scattering centers (atoms) in the sample. The intensity is the modulus squared of $\Psi(\mathbf{Q})$. When you have multiple-scattering centers, the waves scattered from each center may combine coherently or incoherently. In the case of incoherent scattering, the total intensity is simply the sum of the intensities from each atom which can be written as

$$\begin{aligned} I_{\text{inc}} &= \sum_i \psi_i^* \psi_i, \\ &= \sum_i f_i^*(\mathbf{Q}) f_i(\mathbf{Q}). \end{aligned} \quad (3.10)$$

This can be written in terms of a sum over atom types since all information about the relative location of the individual atoms is lost, and therefore, their location is not needed,

$$\begin{aligned} I_{\text{inc}} &= \sum_{\alpha} N_{\alpha} f_{\alpha}^*(\mathbf{Q}) f_{\alpha}(\mathbf{Q}), \\ &= N \sum_{\alpha} c_{\alpha} f_{\alpha}^*(\mathbf{Q}) f_{\alpha}(\mathbf{Q}), \\ &= N \langle f^2 \rangle. \end{aligned} \quad (3.11)$$

From this, we see that the incoherent scattering is given by the number of atoms, N , times the average of the atomic form factors. Here, N_{α} is the number of atoms of type α and $c_{\alpha} = N_{\alpha}/N$. The asterisks indicate complex conjugates. This defines $\langle f^2 \rangle$. Similarly, we can define the sample average scattering power as

$$\langle f \rangle = \sum_{\alpha} c_{\alpha} f_{\alpha}(\mathbf{Q}). \quad (3.12)$$

The square of $\langle f \rangle$ is then

$$\begin{aligned} \langle f \rangle^2 &= \left(\frac{1}{N^2} \right) \sum_{ij} f_j^* f_i, \\ &= \sum_{\beta} \beta c_{\beta} \sum_{\alpha} c_{\alpha} f_{\alpha}^* f_{\beta}, \end{aligned} \quad (3.13)$$

where for notational simplicity we have dropped the explicit reference to the \mathbf{Q} -dependence of f .

If the atoms scatter coherently, what is the intensity in this case? It is given by $\psi^*(\mathbf{Q})\psi(\mathbf{Q})$, thus

$$\begin{aligned} I_c &= \sum_i \sum_j f_j^* f_i \exp(i\mathbf{Q} \cdot (\mathbf{r}_i - \mathbf{r}_j)), \\ &= \sum_{j,i} f_j^* f_i \exp(i\mathbf{Q} \cdot \mathbf{r}_{ij}). \end{aligned} \quad (3.14)$$

We can separate out the self-scattering coming from individual atoms where $i=j$ and $\mathbf{r}_{ij}=0$

$$\begin{aligned}
 I_c &= \sum_i f_i^* f_i + \sum_{i \neq j} f_j^* f_i \exp(i\mathbf{Q} \cdot \mathbf{r}_{ij}), \\
 &= N \langle f^2 \rangle + \sum_{i \neq j} f_j^* f_i \exp(i\mathbf{Q} \cdot \mathbf{r}_{ij}).
 \end{aligned} \tag{3.15}$$

where we have made use of Eq. (3.13). We can define the discrete scattering, I_d , by subtracting the self-scattering from the coherent scattering,

$$\begin{aligned}
 I_d &= I_c - N \langle f^2 \rangle, \\
 &= \sum_{i \neq j} f_j^* f_i \exp(i\mathbf{Q} \cdot \mathbf{r}_{ij}).
 \end{aligned} \tag{3.16}$$

Now, we want to determine $S(\mathbf{Q}) = \frac{I_c}{N \langle f \rangle^2} - \frac{\langle (f-f)^2 \rangle}{\langle f \rangle^2}$, where the numerator of the second term becomes $(\langle f^2 \rangle - \langle f \rangle^2)$. This is the Laue monotonic diffuse-scattering term that comes about because of the imperfect cancellation of intensity at the destructive interference condition when there are scatterers of different strengths present. Note that this term is zero for the case of a single type of scatterer, for X-ray scattering from an elemental material, for example. From Eq. (3.15) we get

$$\frac{I_c}{N} = \langle f^2 \rangle + \left(\frac{1}{N} \right) \sum_{i \neq j} f_j^* f_i \exp(i\mathbf{Q} \cdot \mathbf{r}_{ij}) \tag{3.17}$$

and

$$\frac{I_c}{N} - \langle f^2 \rangle = \left(\frac{1}{N} \right) \sum_{i \neq j} f_j^* f_i \exp(i\mathbf{Q} \cdot \mathbf{r}_{ij}), \tag{3.18}$$

and finally

$$\frac{I_c}{N \langle f \rangle^2} - \frac{\langle f^2 \rangle}{\langle f \rangle^2} = \left[\frac{1}{N \langle f \rangle^2} \right] \sum_{i \neq j} f_j^* f_i \exp(i\mathbf{Q} \cdot \mathbf{r}_{ij}). \tag{3.19}$$

Thus,

$$\begin{aligned}
 S(\mathbf{Q}) - 1 &= \frac{I_c}{N \langle f \rangle^2} - \frac{\langle f^2 \rangle}{\langle f \rangle^2}, \\
 &= \frac{I_d}{N \langle f \rangle^2}, \\
 &= \frac{1}{N \langle f \rangle^2} \sum_{i \neq j} f_j^* f_i \exp(i\mathbf{Q} \cdot \mathbf{r}_{ij}).
 \end{aligned} \tag{3.20}$$

We thus have an expression for $S(\mathbf{Q})$ in terms of scattering from all the atoms in our material.

For an isotropic sample, for example, a powder of crystals or nanoparticles, we assume there to be a crystallite with every orientation with equal

probability and we can take an orientational average. Place the \mathbf{Q} along z in our coordinate system so that $\mathbf{Q} \cdot \mathbf{r}_{ij} = Qr_{ij} \cos \theta$, where θ is the angle between \mathbf{Q} and \mathbf{r}_{ij} . Then the orientational averaging means that \mathbf{r}_{ij} points in all directions with equal probability and θ takes all values with equal probability. The sample-averaged intensity for a pair of atoms will therefore be

$$\begin{aligned} \overline{\exp(i\mathbf{Q} \cdot \mathbf{r}_{ij})} &= \frac{\int_0^{2\pi} d\varphi \int_0^\pi d\theta \exp(iQr_{ij} \cos \theta) r_{ij}^2 \sin \theta}{\int_0^{2\pi} d\varphi \int_0^\pi d\theta r_{ij}^2 \sin \theta}, \\ &= \frac{-2\pi r_{ij}^2 [\exp(iQr_{ij} \cos \theta)]_0^\pi}{4\pi r_{ij}^2 iQr_{ij}}, \\ &= \frac{[\exp(iQr_{ij}) - \exp(-iQr_{ij})]}{2iQr_{ij}}, \\ &= \frac{\sin(Qr_{ij})}{Qr_{ij}}. \end{aligned} \quad (3.21)$$

Substituting $\overline{\exp(i\mathbf{Q} \cdot \mathbf{r}_{ij})}$ for $\exp(i\mathbf{Q} \cdot \mathbf{r}_{ij})$ in Eq. (3.17) results in the well-known Debye (1915) Equation. The structure function for scattering from an isotropic sample is then

$$S(Q) - 1 = \left[\frac{1}{N\langle f \rangle^2} \right] \sum_{i \neq j} f_j^* f_i \left[\frac{\sin(Qr_{ij})}{Qr_{ij}} \right], \quad (3.22)$$

and $F(Q) = Q[S(Q) - 1]$ is

$$F(Q) = \left[\frac{1}{N\langle f \rangle^2} \right] \sum_{i \neq j} f_j^* f_i \left[\frac{\sin(Qr_{ij})}{r_{ij}} \right]. \quad (3.23)$$

For completeness, we describe the removal of the Q -dependence of the X-ray form factors. The form factors are assumed to be isotropic so depend only on Q and not on \mathbf{Q} , which is a good approximation for scattering from core electrons especially. Write $f(Q) = f(0)\tilde{f}(Q)$, where $\tilde{f}(Q)$ has value 1 at $Q = 0$ and contains the Q -dependence of the form factor and $f(0) \sim Z$, where Z is the atomic number that scales the form factor. The Morningstar–Warren (1936) approximation is that the Q -dependent part of the form factors can be well approximated by an average Q -dependence, $\overline{\tilde{f}(Q)} = \left(\frac{1}{N_z} \right) \sum_z c_\alpha \tilde{f}_\alpha(Q)$. In this case, the Q -dependence, $\overline{\tilde{f}(Q)}$,

comes out of the double sums in Eq. (3.23) on the top and the bottom and cancels out. The f s that remain are Q -independent, and normally replaced by the atomic number (modified by any anomalous scattering factors). The same result holds for neutron scattering where the f s are replaced by coherent neutron scattering lengths, b_c . These have no Q -dependence, and therefore, the approximate method for removing the Q -dependence is not needed.

Now, we want to take the inverse Fourier transform, $f(r)$ of $F(Q)$. $F(Q)$ is an odd function so it is a sine Fourier transform,

$$f(r) = \left(\frac{2}{\pi}\right) \int_0^\infty F(Q) \sin(Qr) dQ. \quad (3.24)$$

We choose the $(2/\pi)$ prefactor so that the direct transform has a prefactor of 1. Substituting the expression for $F(Q)$ into the equation and rearranging we get

$$\begin{aligned} f(r) &= \left(\frac{2}{\pi N \langle f \rangle^2}\right) \sum_{i \neq j} \frac{f_j^* f_i}{r_{ij}} \int_0^\infty \sin(Qr_{ij}) \sin(Qr) dQ, \\ &= \left(\frac{1}{N \langle f \rangle^2}\right) \sum_{i \neq j} \frac{f_j^* f_i}{r_{ij}} [\delta(r - r_{ij}) - \delta(r + r_{ij})], \\ &= \left(\frac{1}{r N \langle f \rangle^2}\right) \sum_{i \neq j} f_j^* f_i [\delta(r - r_{ij}) - \delta(r + r_{ij})], \end{aligned} \quad (3.25)$$

which is

$$f(r) = \left(\frac{1}{r N \langle f \rangle^2}\right) \sum_{i \neq j} f_j^* f_i [\delta(r - r_{ij})] \quad (3.26)$$

if we confine ourselves to the physically meaningful positive axis.

We can interpret $f(r)$ in terms of the RDF. The RDF, denoted $R(r)$, is defined for an elemental system such that for an arbitrary atom i at the origin, $R_i(r)dr$ gives the number of atoms in a shell of thickness dr at a distance r from that atom, and the total RDF is the average of the partial RDFs over each atom taken at the origin. Thus, the integral of the RDF between two bounds, a and b , gives the number of atomic pairs per atom with separation within those bounds, N_{ab} . By inspection, we see that Eq. (3.26) yields this behavior if we multiply $f(r)$ by r . For a solid with α atomic species we get

$$\begin{aligned} \int_a^b f(r) r dr &= \int_a^b \left(\frac{1}{N \langle f \rangle^2}\right) \sum_{i \neq j} f_j^* f_i [\delta(r - r_{ij})] dr, \\ &= \left(\frac{1}{N \langle f \rangle^2}\right) \sum_i \sum_{j \in S} f_j^* f_i, \\ &= \left(\frac{1}{\langle f \rangle^2}\right) \sum_\alpha c_\alpha f_\alpha \sum_{j \in S} f_j^*, \end{aligned} \quad (3.27)$$

where S is the set of atoms that lie within a distance $a < r_{ij} < b$. For a single species of scatterer, this reduces to

$$\int_a^b f(r)rdr = \left(\frac{f^2}{f^2}\right) \sum_{j \in S} 1. \quad (3.28)$$

$$= N_{ab}$$

This establishes that $f(r)r$ is indeed $R(r)$, the RDF and

$$f(r) = \frac{R(r)}{r}, \quad (3.29)$$

$$= 4\pi r \rho(r)$$

and not $G(r) = 4\pi r[\rho(r) - \rho_0]$ as previously assumed. Equation (3.4) is strictly incorrect and should be replaced by

$$\frac{R(r)}{r} = 4\pi r \rho(r) = \left(\frac{2}{\pi}\right) \int_0^\infty F(Q) \sin(Qr) dQ. \quad (3.30)$$

As discussed above, the actual experiment is measured only down to a minimum Q value, Q_{\min} . If we rewrite (3.24) now as

$$f(r; Q_{\min}) = \left(\frac{2}{\pi}\right) \int_{Q_{\min}}^\infty F(Q) \sin(Qr) dQ, \quad (3.31)$$

$$= 4\pi r \rho(r) - \left(\frac{2}{\pi}\right) \int_0^{Q_{\min}} F(Q) \sin(Qr) dQ,$$

$$= 4\pi r \rho(r) - L(r).$$

The second term in this expression contains the small-angle scattering; it is the Fourier transform of $F(Q)$ in the very low Q region. A number of different explicit situations are discussed in Farrow and Billinge (2009), and we refer interested readers there for the derivations. For the case that the solid is infinite and of uniform number density, ρ_0 ,

$$L(r) = 4\pi r \rho_0 \quad (3.32)$$

and

$$f(r; Q_{\min}) = G(r) = 4\pi r[\rho(r) - \rho_0], \quad (3.33)$$

the expected result for bulk materials.

For a finite sized solid of uniform density, which has a shape function (defined such that it has a value 1 inside the shape and a value 0 outside the shape) $s(\mathbf{r})$, $L(\mathbf{r}) = 4\pi r \rho_0 \gamma_0(\mathbf{r})$, where $\gamma_0(\mathbf{r})$ is the characteristic function for the objects. This function, well known to small-angle scatterers, is the autocorrelation function of the shape function,

$$\gamma_0(\mathbf{r}) = \left(\frac{1}{V} \right) \int s(\mathbf{r}') s(\mathbf{r}' + \mathbf{r}) d\mathbf{r}'. \quad (3.34)$$

Here, $\gamma_0(\mathbf{r})$ is a three-dimensional shape that must be orientationally averaged for the powder case, as described in more detail in Farrow and Billinge (2009). This then results in the expression

$$f(r; Q_{\min}) = G'(r) = 4\pi r \left[\rho_{\text{object}}(r) - \rho_0 \gamma_0(r) \right]. \quad (3.35)$$

From this, we see that we can calculate a generalized $G(r)$ function (called here $G'(r)$) for a finite sized object by calculating $\rho(r)$ for the finite sized object ($\rho_{\text{object}}(r)$) which sits on top of a smooth background given by $-4\pi r \rho_0 \gamma_0(r)$. At $r=0$, $\gamma_0(r)=1$ and it gradually decreases to zero at $r=d$, where d is the largest dimension of the object, for example, the diameter if it is a sphere. Thus, the “background” on which $\rho(r)$ sits slopes down from 0 at $r=0$ with the initial slope of $-4\pi r \rho_0$, just as in the bulk case, but then curves smoothly back up to $G=0$ at d , at the same place where $\rho_{\text{object}}(r)$ itself goes to zero. This behavior is evident in Fig. 3.3 which shows $G(r)$ from a CdSe nanoparticle. In this case, there are small ripples in the measured $G(r)$ at larger r values which come from density fluctuations in the packing of the nanoparticles (the interparticle correlation function), which is not considered in this treatment.

If the object has a uniform internal structure that can be modeled as a finite piece cut out of a bulk structure, then $\rho_{\text{object}}(r) = \gamma_0(r) \rho_{\text{bulk}}(r)$ (Guinier, 1963) and from Eq. (3.35) we get

$$f(r; Q_{\min}) = G'(r) = 4\pi r \gamma_0(r) [\rho_{\text{bulk}}(r) - \rho_0]. \quad (3.36)$$

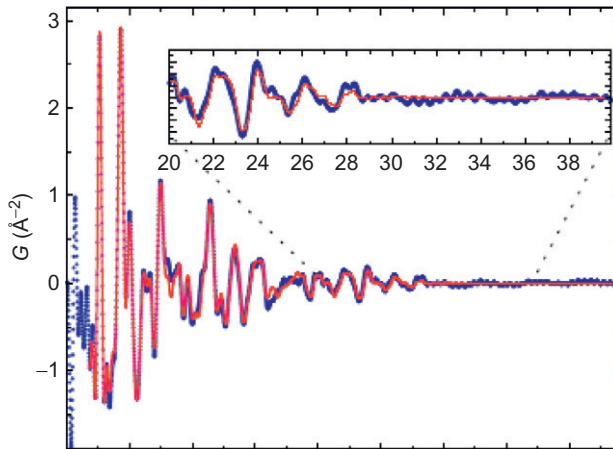


FIGURE 3.3 Symbols are the experimentally determined PDF from small 4-nm diameter CdSe nanoparticles. The solid line is a fit of a model with the Wurtzite crystal structure but where an envelope function of the autocorrelation function of a sphere has been applied, showing the effect on the PDF baseline and $\rho(r)$ oscillations of a finite sized spherical particle (Masadeh *et al.*, 2007).

This is the theoretical justification for the successful practical application of this approach implemented in PDFgui and discussed in [Chapter 6](#). This equation was used to obtain the fit to the nanoparticle data in [Fig. 3.3](#).

[Equations \(3.35\) and \(3.36\)](#) are of great (and will be of increasing) practical value when modeling the measured PDFs of nanoparticles since $\gamma_0(r)$ is known analytically for many shapes and otherwise can be calculated numerically and may be measured directly using small-angle scattering when the particle shape is not known. These equations show how to incorporate the information into the PDF modeling scheme.

It should be noted that these equations are only strictly correct when there is no definite orientational relationship between the shape function and the underlying atomic scale structure encoded in $\rho(r)$. This is often not the case as particles become elongated in particular crystallographic directions. In these cases, the shape and structure are not separable and it is not correct to do the orientational average *before* applying the shape function to the model. In this case, it is straightforward to compute an accurate RDF $R(r)$ and therefore $\rho_{\text{object}}(r)$, from the model, but the background function given by $-4\pi\rho_0\gamma_0(r)$ is approximate. The distortion to this background due to this approximation is expected to be small, but this has not been investigated in detail.

[Equations \(3.35\) and \(3.36\)](#) show nicely how the small-angle scattering data come into the PDF equations. When the small-angle scattering is excluded from the measurement, as it normally is, the resulting correlation function sits on the background $4\pi r\rho_0\gamma_0(r)$ which slopes down from zero but then curves over and comes back up to zero at the size of the nanoparticle, as we mentioned above. The measured $\rho_{\text{object}}^m(r)$ comes from the internal structure of the nanoparticle. This is also zero for r larger than d . However, often $\rho_{\text{object}}^m(r)$ is found to reach 0 at $r < d$ due to structural disorder that limits the structural coherence. The “size” measured from small-angle scattering data and that measured directly from the PDF are different, and this provides crucial information about structural disorder in the nanoparticle. The size deduced from the small-angle scattering gives the physical size of the nanoparticle, whereas that obtained from the PDF is the size of the coherent structural domain or crystallite which may be smaller than the physical size if there is significant surface disorder or incoherent subdomains (grains) in the nanoparticle.

There are analytic solutions for the characteristic functions for certain simple shapes such as spheres, spheroids, ellipsoids, and so on ([Guinier et al., 1955](#); [Qiu et al., 2005](#); [Kodama et al., 2006](#); [Masadeh et al., 2007](#)). For other shapes, and for any arbitrary shape in fact, $\gamma_0(r)$ may be evaluated numerically. The background for the PDF models can also be determined directly by measuring the small-angle scattering and Fourier transforming it as described in [Farrow and Billinge \(2009\)](#). We note that $G(r)$ may be calculated directly in real space or by evaluating the Debye function from a finite object in reciprocal space and then Fourier transforming it to real space. This is the best approach for small particles but becomes prohibitively computationally expensive for even

moderately sized nanoparticles, though there are approximate numerical approaches available for larger particles (Cervellino *et al.*, 2006). Both approaches to calculating $G(r)$ give reliable results and different programs use each approach as discussed in more detail in Chapter 6.

3.1.3. The PDF and All Its Friends and Relations

3.1.3.1. The Pair Distribution Function, $g(r)$, and the Pair Density Function, $\rho(r)$

We have chosen to define the atomic pair distribution function in terms of $g(r)$ in Eq. (1.1). However, there are a host of rather similar correlation functions that the reader is likely to come across. They are mostly related simply by multiplicative and additive constants and contain the same structural information. An excellent Rosetta Stone for deriving each of these functions from one another is Keen (2001). Each has its own properties and advantages and disadvantages which we try and highlight here. It is important to be able to distinguish them in any given situation. Another complication lies in the fact that different authors use different letters for the same function, though it is common practice to define the function in most papers.

As discussed in Section 1.1.4, $g(r)$ is called the pair distribution function. It is normalized so that, as $r \rightarrow \infty$, $g(r) \rightarrow 1$. Also, as we discussed in Chapter 1, as $r \rightarrow 0$ (for r shorter than the distance of closest approach of pairs of atoms) $g(r)$ becomes zero. It is closely related to the pair density function, $\rho(r) = \rho_0 g(r)$. Clearly, $\rho(r)$ oscillates about, and then asymptotes to, the average number density of the material, ρ_0 at high- r and becomes zero as $r \rightarrow 0$. The main advantage of these functions is that they emphasize the low- r short-range order. In a sample with perfect structural coherence (e.g., a perfect crystal), the amplitude of the oscillations (containing the structural information) in these functions falls off like $1/r$. However, when these functions are determined experimentally, the uncertainties in the data also fall off like $1/r$. In this respect, the fact that the low- r structure is emphasized is cosmetic rather than real because the uncertainties in the data (the error bars) scale with the amplitude of the signal. This brings us to our next-correlation function, $G(r)$.

3.1.3.2. The Reduced Pair Distribution Function, $G(r)$

Another widely used correlation function is the reduced pair distribution function, $G(r)$. This is defined as $G(r) = 4\pi r \rho_0 (g(r) - 1)$. From the definition, and our previous discussion, it is clear that this function oscillates around zero in the limit of large r . It also becomes evident by considering the definition that, as $r \rightarrow 0$ this function behaves like $-4\pi \rho_0 r$. That is, at low- r this function is a straight line going through zero with a slope that is proportional to the average number density of the material.

Though less physically intuitive than $g(r)$ itself, this function has some distinct advantages and is very widely used. The main advantage is that this function is the one directly obtained from the Fourier transform of $S(\mathbf{Q})$. It is therefore the function which is most directly related to the data. For example, to obtain either $g(r)$ or $\rho(r)$ from the data, it is necessary to assume a value for the average number density, ρ_0 . This is not necessary in $G(r)$; on the contrary, this information is already contained in $G(r)$ as the slope of the function at low- r . From a philosophical point of view, there is a cleaner separation of data analysis to obtain the correlation function and data modeling to obtain the structural information from that function since there is nothing about the underlying structure that is assumed in obtaining $G(r)$.

A second advantage of $G(r)$, related to the fact that it is the direct Fourier transform of the intensity data, is that the random uncertainties on the data are constant in r . This comes about as a direct result of the error propagation process described later. This has two advantages. The first is sociological. It is common to plot a correlation function calculated from a model on top of the measured one and to plot a difference curve underneath which highlights the differences. Because the uncertainties are constant in r , fluctuations in the difference curve have the same significance at all values of r . Thus, for example, if the fluctuations in the difference curve decrease with increasing r this implies that the model is getting better at longer distances (perhaps it is a model of the average crystallographic structure). This inference cannot be made from a difference curve to $\rho(r)$ or $g(r)$ since we expect the fluctuations to fall off as $1/r$ simply due to the statistical fluctuations. In this case, the reader's eye then has to judge whether the fluctuations are falling off faster or slower than $1/r$ (not an easy task) to judge whether the model is getting better or worse with increasing r .

A danger also lurks when fitting models to $\rho(r)$ or $g(r)$. Unless, a statistically weighted residuals function (often called the A -factor in PDF work) is used, the refinement will be giving statistically unwarranted importance to the low- r data. If $G(r)$ is fit this problem is avoided regardless of whether a weighted or unweighted residual function is used since the statistical uncertainties are constant in r anyway.

A further advantage of the $G(r)$ function is that the amplitude of the oscillations gives a direct measure of the structural coherence of the sample. In a crystal with perfect structural coherence, oscillations in $G(r)$ extend to infinity with a constant peak–peak amplitude. There is a mathematical reason based on the famous (and still unsolved) Gauss circle problem¹ discussed in [Levashov et al. \(2005\)](#), but for a perfectly periodic infinite crystal and a perfect resolution measurement, the oscillations in $G(r)$ continue with constant average amplitude indefinitely in r . This is shown for a calculated curve from fcc nickel in [Fig. 3.4](#). In the $G(r)$ from a real measurement of a crystal, the peak–peak amplitude of the

1. For a summary of what is known about the Gauss Circle Problem, see <http://mathworld.wolfram.com/GaussCircleProblem.html>.

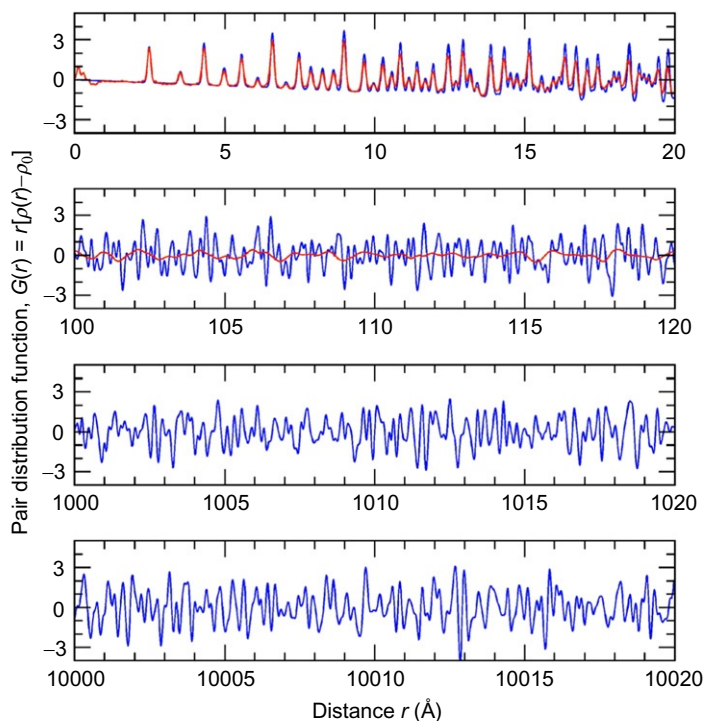


FIGURE 3.4 Calculated PDF, $G(r)$, from fcc nickel. The average peak–peak amplitude is constant however far in r you go. The lowest panel shows features from atoms separated by 10,000 Å or 1 μm . The overlaid plot in the top two panels is the actual measured PDF of nickel from the moderately high-resolution NPDF diffractometer at LANL. The instrumental resolution function results in a loss of feature amplitude already by 12 nm, though higher resolution instruments such as the ID31 X-ray diffractometer at ESRF could measure PDFs to higher- r (Levashov *et al.*, 2005).

signal gradually falls off due to the finite Q -resolution of the measurement, as shown in Fig. 3.4, which is then the limitation on the spatial coherence of the measurement rather than the structural coherence itself. A higher Q -resolution results in data extending over a wider range of r . In samples with some degree of structural disorder, the signal amplitude in $G(r)$ falls off faster than dictated by the Q -resolution and this becomes a useful measure of the structural coherence of the sample. This is nicely illustrated in Fig. 3.5 (Petkov *et al.*, 2000a, b,c). The top panel, (a), shows $G(r)$ from a pristine sample of WS_2 , a layered material with relatively good crystallinity. Figure 3.5b shows the data from a sample where the layers have been ripped apart in solution (so-called exfoliation) and then restacked again. In this case, the structure of the layers has changed as evident by the differences in $G(r)$ at low- r . However, it is also apparent that the signal is dropping off more rapidly with r in the restacked sample.

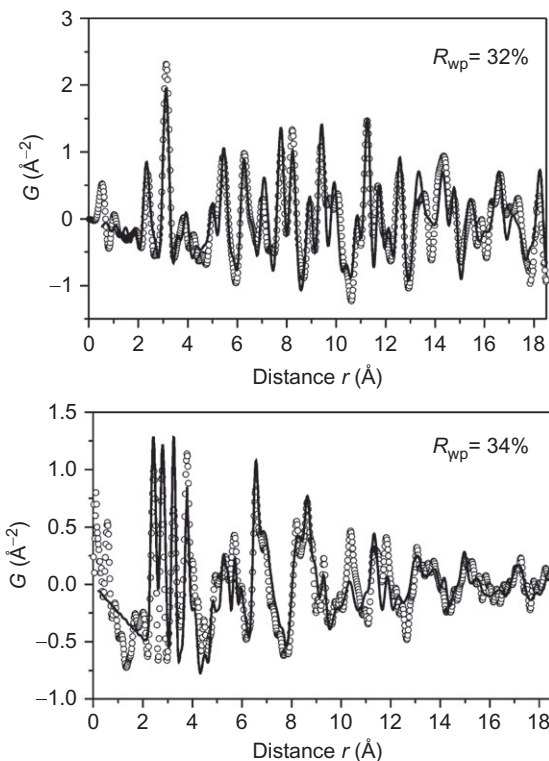


FIGURE 3.5 Top panel: X-ray $G(r)$ of pristine WS_2 ; lower panel: $G(r)$ of reformed sample after exfoliation. Circles are the data, and solid lines are PDFs calculated from structural models. Note that the amplitude of the ripples in $G(r)$ dies out in the nanocrystalline reformed sample (Petkov *et al.*, 2000a,b,c).

This means that, even within the layers, the structure is more disordered and there is less structural coherence. These restacked samples are metastable and decay back to the highly ordered pristine structures over a period of time.

There is one final feature of $G(r)$, again related to its experimental importance. In a real experiment, $S(Q)$ is measured only over a finite range of Q . The consequence in the Fourier transform is that termination ripples appear; ripples with a wavelength $\sim 2\pi/Q_{\text{max}}$. Mathematically, this comes about because the theoretical $G(r)$ becomes convoluted with the Fourier transform of the termination function. This is discussed in more detail in Section 3.5. For completeness, we simply make the point that it is $G(r)$ that should be thus convoluted, not $\rho(r)$ or $g(r)$.

3.1.3.3. The Radial Distribution Function, $R(r)$

The next-correlation function we discuss is the most physically intuitive. The PDF, $g(r)$, is related to the RDF, $R(r)$, by

$$R(r) = 4\pi r^2 \rho_0 g(r). \quad (3.37)$$

The RDF has the useful property that the quantity $R(r)dr$ gives the number of atoms in an annulus of thickness dr at distance r from another atom. For example, the coordination number, or the number of neighbors, N_C , is given by

$$N_C = \int_{r_1}^{r_2} R(r)dr, \quad (3.38)$$

where r_1 and r_2 define the RDF peak corresponding to the coordination shell in question. This suggests a scheme for calculating PDFs from atomic models. Consider a model consisting of a large number of atoms situated at positions \mathbf{r}_v with respect to some origin. Expressed mathematically, this amounts to a series of delta functions, $\delta(\mathbf{r} - \mathbf{r}_v)$. The RDF is then given as

$$R(r) = \sum_v \sum_{\mu} \frac{b_v b_{\mu}}{\langle b \rangle^2} \delta(r - r_{v\mu}). \quad (3.39)$$

Here, the b values are the atomic scattering lengths of the ions and the sums are over every atom in the sample. This is a restatement of Eq. (1.1), and indeed, this property of $R(r)$ is the origin of that equation. In the case of X-rays, the b values are replaced by $f_v(0)$, the value of the atomic scattering factor for the v th atom at $Q=0$. Note that $f_v(0) \sim Z_v$, the atomic number of the species. The value $r_{v\mu} = |\mathbf{r}_v - \mathbf{r}_{\mu}|$ is the magnitude of the separation of the v th and μ th ions. The angle brackets are an average over all atoms (and isotopes) in the model.

The RDF has the other useful property that peaks in the function coming from well-defined atom–atom pairs reflect the precise shape of the pair-probability distribution. In the harmonic approximation (which is rather well obeyed in most cases), these peaks will have a Gaussian shape in the RDF.²

In the other distribution functions, we describe they are close to, but not exactly, Gaussian. The disadvantage of $R(r)$ is that it diverges (like r^2) with increasing r making it less satisfactory to plot if the structure is being considered over an extended range of r .

A number of other correlation functions come about because of different definitions of partial structure functions in multicomponent systems. A discussion of these will be left until later. A thorough comparison of different correlation function conventions has been made recently (Keen, 2001).

3.1.4. Brief History

As early as 1915, Debye (Debye, 1915) took a three-dimensional average of the sample structure amplitude (Eq. 2.7) to obtain the scattering expected from an isotropic sample such as an amorphous material or a powder. The formalism of correlation functions was introduced later and Zernicke and Prins (1927)

2. Even in the case of Gaussian probability distributions, small modifications to the Gaussian line shape come from the three-dimensional powder averaging process, especially in the case of anisotropic thermal motions, as pointed out by Dimitrov *et al.* (2001) and discussed by Thorpe *et al.* (2002). These corrections are small but need to be taken into account for the greatest accuracy.



FIGURE 3.6 Picture of Beevers–Lipson strips (American Crystallographic Association).

showed the famous relationship between the two-point atom-pair correlation function and the isotropically averaged scattering function that we give in Eq. (3.4). At the time, there were no high-speed computers. Nonetheless, the approach was applied as early as 1930 by Debye and Menke to study liquid mercury. Significant early work was done with the method by Warren and coworkers (Tarasov and Warren, 1936; Warren *et al.*, 1936) by inverting the data manually using Beevers–Lipson strips, a device as unfamiliar to modern science as the slide rule. Pictures of Beevers–Lipson strips are shown in Fig. 3.6, and a short description of their use is presented in Appendix 3.1. Needless to say it was a tedious and time-consuming affair and the approach was not widely embraced. In the 1960s, computers, often with charming names,³ began to be used in an increasing number of studies (e.g., Henshaw, 1960³; Clayton and LeRoy, 1961³; Kaplow *et al.*, 1964, 1968; Ocken and Wagner, 1966), including studies of polycrystalline materials (Ruppersberg and Seemann, 1965; Fessler *et al.*, 1966; Temkin, 1973).

The technique may have played a part in one of the most famous and controversial of all Nobel prizes. James Watson and Francis Crick were awarded the 1962 Nobel prize for chemistry for solving the double-helix structure of DNA. The breakthrough came in 1953 at Cambridge University. Their main competitors, Maurice Wilkins and Rosalind Elsie Franklin, were at the University of London. Rosalind Franklin had superb X-ray diffraction data from DNA (J.D. Bernal called her X-ray photographs of DNA, “the most beautiful X-ray

3. The computer used to transform the Henshaw data was named the “Datatron” and located at Chalk River Laboratories in Canada. The Clayton and LeRoy data were transformed by “George” at Argonne National Laboratory!

photographs of any substance ever taken”). While Franklin struggled to analyze the data using crystallographic analysis, including Fourier methods that Franklin was well familiar with from her studies of carbon (Section 9.3.2), Crick and Watson came up with their insightful, simple, and elegant solution to the scattering data using model building and chemical intuition. It is interesting that Watson had his insight only after being shown one of Franklin’s excellent diffractograms of DNA; they had no X-ray data of their own. Sadly, in 1958, at the age of 37 and 4 years before Crick and Watson won their Nobel prize, Franklin died of ovarian cancer. Rather differing accounts of the controversy surrounding Franklin’s role in the discovery of the structure of DNA can be read in Watson’s book (2001), *The Double Helix; A Personal Account of the Discovery of the Structure of DNA*, Rosalind Franklin: *The Dark Lady of DNA* by Maddox (2002), and *Rosalind Franklin and DNA* by Sayre (2000).

As computers got faster and more widely available in the 1960s and 1970s, the application of the technique in the areas of liquids and amorphous materials grew immensely (Klug and Alexander, 1968; Warren, 1969). However, the technique was not widely applied to crystalline materials. At the same time, computers were also applied in the analysis of crystallographic data, for example, with the development of the Rietveld refinement of powder diffraction data. There seemed little point in Fourier transforming diffraction data to obtain $G(r)$ when you could learn everything directly from the diffraction pattern, including the space-group symmetry, unit-cell size, and with the advent of quantitative Bragg peak analyses such as Rietveld analysis and atomic positions. PDFs were low-resolution affairs blighted by spurious ripples which came from the Fourier transform (termination errors, discussed in Section 3.5.2 and Appendix 3.2) and which people went to elaborate lengths to reduce artificially (Kaplow *et al.*, 1964; Konnert and Karle, 1973). These large amplitude artificial ripples had a similar frequency to the data themselves and could be mistaken for real atomic correlations: the “fools gold” of the PDF world. PDF analysis was the technique of last resort, used only in situations when crystallography was inapplicable.

The power of the PDF in the study of liquids and amorphous materials was recognized, but even here there were problems. A case in point was the study of amorphous selenium. The PDF of a-Se was first collected as early as 1942 by Hendus (1942). New datasets from a-Se appeared at a rate of about one per decade (Grimminger *et al.*, 1955; Krebs and Schultze-Gebhardt, 1955; Andrievskii *et al.*, 1960; Henninger *et al.*, 1967) until the late 1960s. Despite this, no consensus emerged even on basic facts such as whether the structure was made of rings or chains. In 1968, the MIT group of Kaplow and Averbach, pioneers of computer-based PDF work, took over. They were forced to bemoan that “there is no general agreement on the structure of amorphous selenium . . . the interpretation of the diffraction data is severely limited by the spurious detail in the experimental distribution functions . . . it frequently appears that the methods of amorphous structure determination are being developed along with the structure” (Kaplow *et al.*, 1968). The MIT group attempt to resolve the situation

involved an iterative computer-based data analysis procedure to get high-quality PDFs and, to our knowledge, the first example of a reverse Monte Carlo modeling analysis. Research continued over the decades and as recently as 1999 a letter appeared in *Physical Review Letters* discussing the structure of a-Se, which turns out to be ideal as a photoreceptor material in photocopiers. Now the bottleneck appears to be the ability to create reliable *ab initio* computer models of a-Se rather than with the PDF data themselves. In this 1999 study, calculated PDFs were compared to data collected in 1982 (Bellissent, 1982), and to the venerable data of Kaplow *et al.*, from 1968!

Termination ripples, and other artifacts coming from improper data normalization (which is another problem associated with low- Q_{\max} values), are not a problem if data are measured to high enough Q_{\max} values. The reason is that, as discussed in Chapter 2, the signal in the real $S(\mathbf{Q})$ dies off due to the Debye–Waller factor. Terminating the data at more than ~ 3 times the standard deviation of the Debye–Waller envelope results in small termination ripples and more reliable data normalization (Toby and Egami, 1992). This is dramatically demonstrated in Section 9.2.6 where PDFs of disordered carbon from data taken by Rosalind Franklin in 1950 are compared with PDFs from modern data. Since in Eq. (2.2), $\sin \theta$ takes a maximum value of 1, and Q_{\max} is $4\pi/\lambda$. To obtain higher Q_{\max} s, it is necessary to use short-wavelength particles. This means higher energy X-rays and epithermal neutrons. Widely available laboratory X-ray sources such as Cu K α give $Q_{\max} \sim 8 \text{ \AA}^{-1}$ and Mo K α gives $Q_{\max} \sim 16 \text{ \AA}^{-1}$, whereas data in excess of $Q = 30 \text{ \AA}^{-1}$ are required, in general. Similar limitations apply to reactor-based thermal neutron sources. It has been the advent of synchrotron-based X-ray sources and spallation neutron sources (as well as affordable high-speed computing) that has revolutionized our ability to measure highly accurate PDFs. The PDF is no longer a technique of last resort and, as applied to crystals, yields important complementary information to a traditional crystallographic analysis (Egami, 1990).

At first glance, electrons are not a good probe for PDF work since the PDF equations are based on the kinematical scattering equations that are relevant for weak scatterers such as neutrons and X-rays, not strong scatterers such as electrons. This is why, despite the fields of electron diffraction and PDF analysis coexisting side by side for 85 years (the first electron diffraction was observed in 1927; Davisson and Germer, 1927; Thomson and Reid, 1927), the same year that Zernike and Prins published their paper showing the Fourier relationship between X-ray diffraction and the real-space pair correlation function (Zernicke and Prins, 1927) the cross talk between the fields has been very limited. The main area where electrons played a part in PDF analysis was where the strong scattering was a clear advantage rather than disadvantage: in the area of gas-phase electron diffraction from molecules, itself first demonstrated in 1930 (Mark and Wierl, 1930). This field, where molecules (and more recently small atomic clusters) in the gas phase at low densities are illuminated by electrons, has a long and rich history which we do not have space to delve into here. It is used to find the structures

of molecular species. A new chapter is emerging in this area with ultrafast time-resolved diffraction measurements of excited states and reaction intermediates of these molecular species (Zewail, 2006). In this method, a femtosecond-pulsed laser is used both to excite the molecules and to excite the electron emission of the field emission tip of the electron source with a fixed time lag. In this way, the time evolution of the molecular structure in the excited state can be followed stroboscopically by taking snapshots at different time delays.

The next area where electron-diffraction-derived PDFs has made an impact is in the study of thin amorphous films. This began with the work of Moss and Graczyk (1969) but has been widely developed and applied since then, not least through the work of Cockayne (Cockayne and McKenzie, 1988; Cockayne, 2007). Two things make this approach viable, despite the strong scattering of the electrons. The first is that thin amorphous films are studied: the shorter the path length of the electrons through a material, the lower the probability of multiple-scattering events. However, possibly more important is the incoherence of the structure itself. Dynamical scattering corrections become relevant when multiple-scattering events occur within the coherence volume of the scattering. If multiple-scattering events are incoherent, the multiple scattering produces an incoherent, slowly varying, background intensity that may be subtracted and the remaining coherent intensity retains its kinematical form. PDF analysis of amorphous materials from electron diffraction remains a relatively small field, but nonetheless useful, for example, when it is not possible to obtain materials in the bulk form, as with $\text{Ge}_2\text{Sb}_2\text{Te}_8$ phase change materials used in writable DVD technologies (Borisenko *et al.*, 2009). A recent development of particular note in this area is the development of fluctuation electron microscopy (Treacy and Gibson, 1996) which provides information about fourth-order correlations in materials that can be used to complement the two-body information found in PDF measurements (Treacy and Borisenko, 2012). The second is the deconvolution of the effects of convergent electron beams that allow very small sample volumes in the amorphous material to be probed. It was recently shown that, even from well-ordered materials such as nanoparticles, under certain circumstances, the dynamical scattering effects can be overcome such that quantitatively reliable PDFs, which can be modeled using standard PDF modeling programs such as PDFgui, can be obtained from laboratory electron microscopes (Abeykoon *et al.*, 2012). Because of the ease of carrying out these experiments, the ubiquity of this kind of microscope and the straightforward data processing this approach for obtaining PDFs from nanomaterials is expected to grow in the future and so these experiments and the data analysis are described in Chapters 4 and 5.

3.1.5. Multicomponent Systems

The equations relating $S(Q)$ and $G(r)$ given above, and the definition of $g(r)$ in Eq. (1.1), are quite general. However, when the system under study is composed of more than one kind of atom, it is generally desirable to understand

the distinct structure about a particular chemical species. If the local coordination environment of a particular chemical species is well defined, this may also allow us to simplify the double sum in Eq. (1.1). In the original definition, Eq. (1.1), the double sum is taken over all the atoms in the solid. We can define a partial pair distribution function, $g_{\alpha\beta}(r)$, that gives the distribution of atom pairs in the material coming only from atoms of type β around atoms of type α (Faber and Ziman, 1965; Waseda, 1980; Suzuki, 1987). Starting from Eq. (1.1), we could define this as $g'_{\alpha\beta}(r) = \frac{1}{4\pi N \rho_0 r^2} \sum_{v \in \{\alpha\}} \sum_{\mu \in \{\beta\}} \delta(r - r_{v\mu})$, in which case the total pair distribution function derived in Eq. (1.1) would clearly be

$$g(r) = \sum_{\alpha} \sum_{\beta} g'_{\alpha\beta}(r). \quad (3.40)$$

The normalized total scattering from the entire ensemble will be given by the contributions from each partial,

$$S(Q) = \sum_{\alpha} \sum_{\beta} S'_{\alpha\beta}(Q). \quad (3.41)$$

This shows intuitively how a total distribution function can be built up from a superposition of different subdistributions.

Although perfectly valid, these definitions for the partial distribution functions and partial structure functions are not unique and indeed are not the widely used standards. The most usual form for these partials is due to Faber and Ziman (1965). As we have discussed, in the limit of large Q , $S(Q) \rightarrow 1$. From Eq. (3.41), it is clear that $\sum_{\alpha} \sum_{\beta} S'_{\alpha\beta}(Q) \rightarrow 1$ in the high- Q limit and the scattering from each partial, $S'_{\alpha\beta}(Q) \rightarrow \langle b_{\alpha\beta} \rangle^2 / \langle b \rangle^2$, the ratio of the scattering cross section of the partial to that of the sample as a whole. It is convenient to take this weighting factor out of the definition for the partial structure functions giving us the Faber–Ziman definition:

$$S_{\alpha\beta}(Q) = \frac{\left(\sum_{\alpha} c_{\alpha} b_{\alpha}\right)^2}{c_{\alpha} c_{\beta} b_{\alpha} b_{\beta}} S'_{\alpha\beta}(Q), \quad (3.42)$$

where it can be readily verified that $\langle b_{\alpha\beta} \rangle^2 = c_{\alpha} c_{\beta} b_{\alpha} b_{\beta}$. The Faber–Ziman partial structure functions have the property that, like the total structure function, they tend to unity as $Q \rightarrow \infty$ (i.e., they are the $S(Q)$ that you would measure if your entire sample was made of only that partial). The total structure function is then given by

$$S(Q) = \sum_{\alpha} \sum_{\beta} \frac{c_{\alpha} c_{\beta} b_{\alpha} b_{\beta}}{\left(\sum_{\alpha} c_{\alpha} b_{\alpha}\right)^2} S_{\alpha\beta}(Q). \quad (3.43)$$

As a result of this normalization, the partial reduced pair distribution function can be obtained as a Fourier transform of the partial structure function,

$$G_{\alpha\beta}(r) = \frac{2}{\pi} \int_0^\infty Q [S_{\alpha\beta}(Q) - 1] \sin(Qr) dQ, \quad (3.44)$$

and substituting Eq. (3.43) into Eq. (3.4) it is readily seen that

$$G(r) = \sum_{\alpha\beta} \frac{c_\alpha c_\beta b_\alpha b_\beta}{\langle b \rangle^2} G_{\alpha\beta}(r). \quad (3.45)$$

Similarly, in this formalism

$$g_{\alpha\beta}(r) = \frac{\left(\sum_\alpha c_\alpha b_\alpha\right)^2}{c_\alpha c_\beta b_\alpha b_\beta} g'_{\alpha\beta}(r) = \frac{1}{4\pi N \rho_0 r^2} \frac{\left(\sum_\alpha c_\alpha b_\alpha\right)^2}{c_\alpha c_\beta b_\alpha b_\beta} \sum_{v \in \{\alpha\}} \sum_{\mu \in \{\beta\}} \delta(r - r_{v\mu}) \quad (3.46)$$

and the total distribution function,

$$g(r) = \sum_{\alpha\beta} \frac{c_\alpha c_\beta b_\alpha b_\beta}{\langle b \rangle^2} g_{\alpha\beta}(r). \quad (3.47)$$

Note that the measured coordination number (Eq. 3.38) also is a weighted sum of the coordination number of each pair,

$$N_C = \sum \frac{c_\alpha c_\beta b_\alpha b_\beta}{\langle b \rangle^2} N_C^{\alpha\beta}(r), \quad (3.48)$$

where $N_C^{\alpha\beta}$ denotes the number of β atoms around an α atom. In the case of X-rays, an approximation has to be made, since the structure function is given by

$$S(Q) = \sum_{\alpha\beta} \frac{c_\alpha c_\beta f_\alpha(Q) f_\beta(Q)}{\langle f(Q) \rangle^2} S_{\alpha\beta}(Q), \quad (3.49)$$

and the weighting factor, $w_{\alpha\beta} = c_\alpha c_\beta f_\alpha(Q) f_\beta(Q) / \langle f(Q) \rangle^2$, is a function of Q . Thus, the total PDF is not exactly the weighted sum of partial PDFs. It can be made to approximate this situation by separating the absolute value and the Q -dependence of $f(Q)$. This is the so-called Morningstar–Warren approximation (Warren *et al.*, 1936). First the Q -dependence of the average form factor is found,

$$\bar{f}(Q) = \frac{\sum_\alpha c_\alpha f_\alpha(Q)}{\sum_\alpha c_\alpha f_\alpha(0)}, \quad (3.50)$$

where $f_\alpha(0) \cong Z_\alpha$ is the atomic number of the α th element. The approximation is then made that $f_\alpha(Q) = Z_\alpha \bar{f}(Q)$. The weighting factors $w_{\alpha\beta}$ are a slowly varying function of Q and, as poor as this approximation is, it does not pose a serious problem in practice. This is largely borne out by how successfully X-ray PDFs from multicomponent systems can be fit by structural models.

For binary systems, the method by Bhathia and Thornton (1970) provide very useful insight. In this method, partial structure functions are rearranged

so that $S(Q)$ is expressed as the sum of terms representing density correlation, $S_{NN}(Q)$, compositional correlation, $S_{CC}(Q)$, and density–composition correlation, $S_{NC}(Q)$,

$$S(Q) = S_{NN}(Q) + 2 \frac{\Delta b}{\langle b \rangle} S_{NC}(Q) + \left(\frac{\Delta b}{\langle b \rangle} \right)^2 S_{CC}(Q), \quad (3.51)$$

where

$$\begin{aligned} \langle b \rangle &= c_A b_A + c_B b_B, \quad \Delta b = |b_A - b_B|, \\ S_{NN}(Q) &= c_A^2 S_{AA}(Q) + 2c_A c_B S_{AB}(Q) + c_B^2 S_{BB}(Q), \\ S_{NN}(Q) &= c_A c_B [c_A S_{AA}(Q) - (c_A - c_B) S_{AB}(Q) - c_B S_{BB}(Q)], \\ S_{NN}(Q) &= c_A c_B [S_{AA}(Q) + S_{BB}(Q) - 2S_{AB}(Q) + 1]. \end{aligned} \quad (3.52)$$

The corresponding PDF and RDF are expressed as the Fourier transform of each term. By integrating the RDF over the first peak, we obtain coordination numbers, $N_C(\text{NN})$ and $N_C(\text{CC})$. The ratio is the so-called Warren chemical or compositional short-range order parameter (Warren *et al.*, 1951),

$$\alpha = \frac{N_C(\text{NN})}{N_C(\text{CC})}. \quad (3.53)$$

The value of α is zero for a completely random alloy, but positive for a system with segregation tendency, and negative for a system with AB association tendency. Chemical affinity between two elements results in a negative Warren order parameter.

3.2. COMPOSITIONALLY RESOLVED PARTIAL PDF

As we have discussed, it is often true that the three-dimensional structure of a material under study can be recovered from the total PDF by quantitative structural modeling. However, the total PDF is basically blind to chemistry, and this presents a major problem in mixed systems. For instance the same crystallographic site is occupied by two chemical species it is difficult to identify the weight of each species unless there is a significant difference in the atomic size as shown in Fig. 1.3. Usually it is desirable to determine the structure explicitly around a particular chemical species through diffraction experiments. In this section, we describe how compositionally resolved PDFs can be determined in practice.

3.2.1. Differential PDF

In Section 3.1.5, we showed that $G(r)$ can be defined as a sum of partial PDFs which are correlation functions between chemically distinct species. The partial PDFs, often referred to simply as partials, have a special physical significance since it is often the case that the relationship between particular chemical species and their neighbors is of interest.

In order to determine all the partial PDFs of a system composed of n elements, one needs a set of at least $n(n-1)/2$ independent $S(\mathbf{Q})$ data determined by diffraction measurements. Moreover, the measured $S(\mathbf{Q})$ often are very similar to each

other, and information is hidden in small differences among the data, thus tending to suffer strongly from noise. Thus, a dataset of extremely high quality is required in order to determine the partials, and even in such a case, it is an extremely difficult task. Nonetheless, in liquids and amorphous materials, this approach is necessary and successfully undertaken (Soper, 2000; Petri *et al.*, 2001). Closely related “differential PDFs” (DDFs) are experimentally much more accessible using differential techniques as we discuss below (Fuoss *et al.*, 1981). DDFs over narrow ranges of r can be obtained by the EXAFS measurement. This is one of the great strengths of the EXAFS technique, which yields chemical specific local structural information. The relative merits and complementarities of the EXAFS and PDF approaches are discussed in Appendix 3.3. In general, the EXAFS measurement is much easier to carry out, while a diffraction measurement provides DDFs over a much wider range of distances than the EXAFS method can. Data interpretation is also more direct in the diffraction method because of the kinematical scattering.

The DDF is the pair correlation function between all atoms and a particular chemical species that can be thought to be located at the origin:

$$G_{\alpha}(r) = \sum_{\beta} \frac{c_{\beta} b_{\beta}}{\langle b \rangle} G_{\alpha\beta}(r). \quad (3.54)$$

For example, an AB alloy will have A–A, B–B, and A–B partials and it will have A and B differentials, where the A differential is the A–A + A–B partials and the B differential is the B–B + B–A partials. In terms of DDFs, the total PDF is given by

$$G(r) = \sum_{\alpha} \frac{c_{\alpha} b_{\alpha}}{\langle b \rangle} G_{\alpha}(r). \quad (3.55)$$

The DDF is related to the differential structure function (DSF),

$$S_{\alpha}(Q) = \sum_{\beta} \frac{c_{\beta} b_{\beta}}{\langle b \rangle} S_{\alpha\beta}(Q) \quad (3.56)$$

through the Fourier transformation,

$$G_{\alpha}(r) = \frac{2}{\pi} \int_0^{\infty} Q [S_{\alpha}(Q) - 1] \sin(Qr) dQ. \quad (3.57)$$

The DSF is related to the total structure function by

$$S(Q) = \sum_{\alpha} \frac{c_{\alpha} b_{\alpha}}{\langle b \rangle} S_{\alpha}(Q). \quad (3.58)$$

3.2.2. Anomalous X-Ray Scattering

The scattering factor of an atom is nearly independent of the energy of X-rays except in the vicinity of the absorption edge of the atom where it depends rather strongly on the X-ray energy E ,

$$f(Q, E) = f_0(Q) + f'(E) + if''(E). \quad (3.59)$$

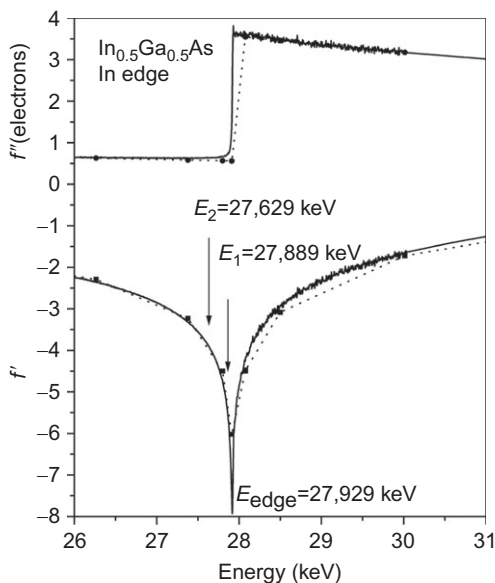


FIGURE 3.7 The anomalous dispersion of In scattering factors calculated near the K absorption edge. Top: imaginary part, f'' ; bottom: real part, f' (Petkov *et al.*, 2000c).

An example of the energy dependence of f' is shown in Fig. 3.7. This energy dependence is known as anomalous dispersion and originates from the resonance of the X-ray with the excitation of electrons in the core of an atom. Thus, if one tunes the X-ray energy to the edge of an element, the scattering power from that particular element varies strongly with energy, while the scattering from other elements remain more or less constant. We can take advantage of this special nature of the interaction between an atom and X-ray to determine the differential and partial PDFs. By carrying out the measurement at two or more energies in the vicinity of the edge of the element α , the scattering power $f_\alpha(Q)$ of the α atoms change but those of the other constituent ions do not. By taking the derivative of $S(Q)$ with respect to $f_\alpha(Q)$,

$$\frac{\partial S(Q)}{\partial f_\alpha(Q)} = \frac{c_\alpha}{\langle f(Q) \rangle} \sum_\beta \frac{c_\beta f_\beta(Q)}{\langle f(Q) \rangle} S_{\alpha\beta}(Q) = \frac{c_\alpha}{\langle f(Q) \rangle} S_\alpha(Q), \quad (3.60)$$

we get an expression for the DSF with respect to element α . This is why $S_\alpha(Q)$ and $G_\alpha(r)$ are called “differential” SF and PDF. Thus, the DSF can be determined by measuring $S(Q)$ from the sample at two photon energies. Even though f' changes most rapidly right at the edge, it is advisable to stay a little away from the edge. The reason is that the absorption factor changes so rapidly near the edge and makes the absorption correction very difficult since the difference in the total scattering measured at two energies is usually rather small. For this reason, and to minimize fluorescence from the sample, it is strongly advised

to stay below the absorption edge of the sample. Examples of a DSF and a DDF determined by anomalous scattering are shown in Figs. 3.8 and 3.9 (Petkov *et al.*, 2000a,b,c).

By determining the second derivative, we obtain the partial structure function,

$$\frac{\partial^2 S(Q)}{\partial f_\alpha(Q) \partial f_\beta(Q)} = \frac{c_\alpha c_\beta}{\langle f(Q) \rangle^2} S_{\alpha\beta}(Q). \quad (3.61)$$

However, the experimental accuracy of the second derivative is low, making the determination of the full partials extremely difficult. For this reason, such a feat is rarely attempted, with some successes for relatively simple systems (Waseda, 1980, 1993). Actually, physical understanding of the atomic environment can be achieved pretty well by knowing the DDFs alone (Price and Saboungi, 1998). If the DDF (or even the total PDF) shows several distinct peaks, it is often not difficult to assign the chemical identity to each peak knowing the atomic radii.

3.2.3. Isotopic Substitution

Elements found in nature are usually composed of various nuclear isotopes which differ from each other in the number of neutrons in the nucleus. While isotopes have almost identical chemical properties and result in virtually the

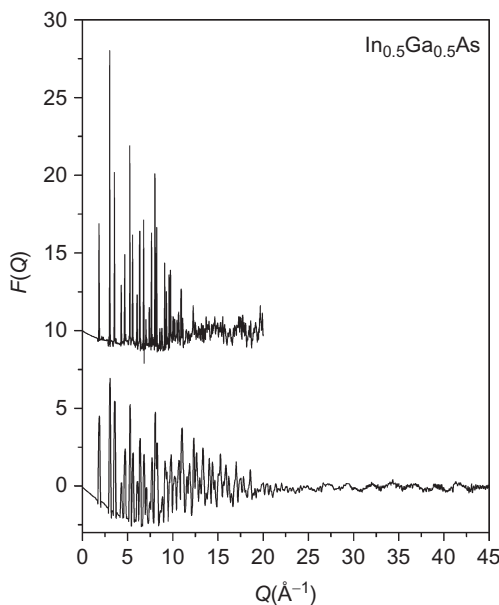


FIGURE 3.8 (Top) The In-differential structure function of $\text{In}_{0.5}\text{Ga}_{0.5}\text{As}$ determined at the In K -edge and (bottom) the total-scattering function, both plotted as $F(Q) = Q[S(Q) - 1]$ (Petkov *et al.*, 2000c).

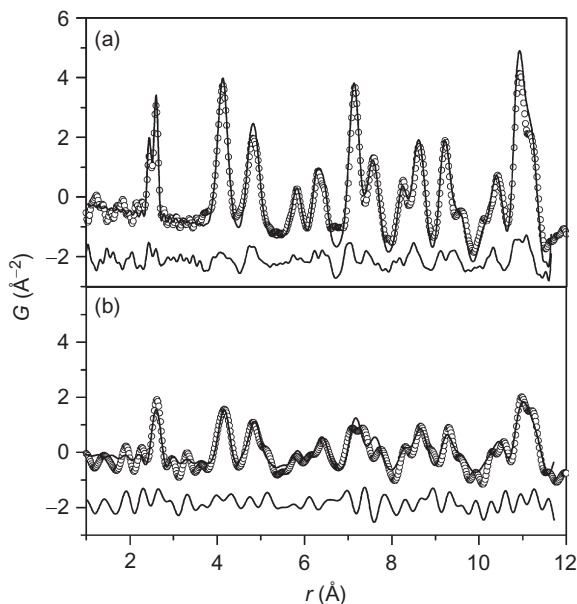


FIGURE 3.9 Total PDF of $\text{In}_{0.5}\text{Ga}_{0.5}\text{As}$ (a) and In-DDF (b) from the data in Fig. 3.6. Open circles are the data, solid lines are calculated from a model (Petkov *et al.*, 2000c). This confirms that the higher- r peak in the nearest neighbor doublet at ~ 2.5 \AA originates from In–As bonds. Here, a high-resolution total PDF and chemically resolved DPDF were both fit with the same structural model further constraining the structural solution.

same structure in the solid state, they can have different neutron scattering lengths. For instance, the value of b for ^{63}Cu is 6.43 fm, while that for ^{65}Cu is 10.61 fm. Thus by obtaining the total neutron PDF for two samples with identical chemical composition and structure but made of two different isotopes, one can determine the DDFs. Let us assume that one has a sample with the isotope 1 of an element α . The total structure function will be given by

$$S_1(Q) = \frac{1}{\langle b_1 \rangle^2} \left[(c_\alpha b_{\alpha 1})^2 S_{\alpha\alpha}(Q) + 2c_\alpha b_{\alpha 1} \sum_{\beta \neq \alpha} c_\beta b_\beta S_{\alpha\beta}(Q) + \sum_{\beta \neq \alpha} c_\beta c_\gamma b_\beta b_\gamma S_{\beta\gamma}(Q) \right], \quad (3.62)$$

where $b_{\alpha 1}$ is the scattering length of the α isotope 1, and

$$\langle b_1 \rangle = c_\alpha b_{\alpha 1} + \sum_{\beta \neq \alpha} c_\beta b_\beta. \quad (3.63)$$

Thus by carrying out the measurement with α isotopes 1 and 2, the difference in the intensity is

$$\begin{aligned}
\Delta I(Q) &= \langle b_1 \rangle^2 S_1(Q) - \langle b_2 \rangle^2 S_2(Q), \\
&= c_\alpha^2 (b_{\alpha 1}^2 - b_{\alpha 2}^2) S_{\alpha\alpha}(Q) + 2c_\alpha (b_{\alpha 1} - b_{\alpha 2}) \sum_{\beta \neq \alpha} c_\beta b_\beta S_{\alpha\beta}(Q), \\
&= 2c_\alpha (b_{\alpha 1} - b_{\alpha 2}) c_\alpha b_\alpha S_{\alpha\alpha}(Q) + 2c_\alpha (b_{\alpha 1} - b_{\alpha 2}) \sum_{\beta \neq \alpha} c_\beta b_\beta S_{\alpha\beta}(Q), \\
&= 2c_\alpha (b_{\alpha 1} - b_{\alpha 2}) S_\alpha(Q),
\end{aligned} \tag{3.64}$$

where $b\alpha = (b\alpha_1 + b\alpha_2)/2$. Thus, the DSF, therefore DDF, can be determined by using two isotopes. In principle, by using isotopes of various elements and carrying out a required number of measurements, all the partial PDFs can be determined. However, the accuracy deteriorates as the number of elements involved is increased. An example of the DDF determined for Cu in $\text{YBa}_2\text{Cu}_3\text{O}_{6.93}$ by using ^{63}Cu and ^{65}Cu is shown in Fig. 3.10 (Louca *et al.*, 1999).

The greatest shortcoming of this technique is that the isotopically separated elements are expensive. Since neutron scattering experiments require samples weighing 10 g or more, the cost of isotopes to produce such samples can be very significant. Also sometimes, isotopes do not show sufficient differences in scattering length, such as ^{16}O ($b = 5.803$ fm) and ^{18}O ($b = 5.84$ fm). Another problem is that two samples with different isotopes may not be identical in structure, especially if the sample preparation is difficult. In fact, the vibrational frequency of the lattice depends on the atomic mass so that the isotopically substituted samples do not have the same Debye–Waller factor. In spite of these

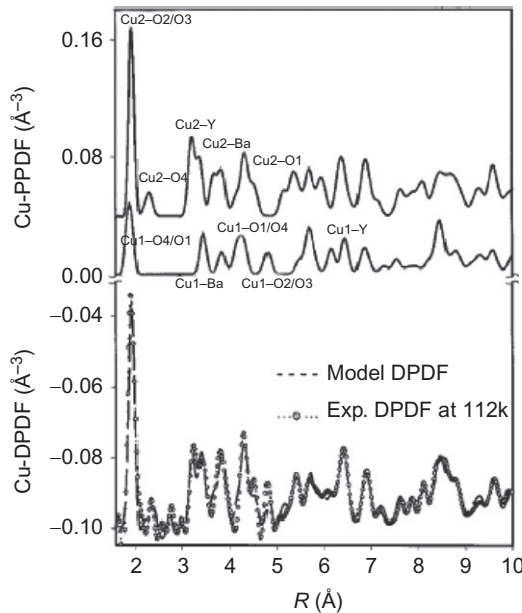


FIGURE 3.10 The DDF determined for Cu in $\text{YBa}_2\text{Cu}_3\text{O}_{6.93}$ by using ^{63}Cu and ^{65}Cu . Data are the dots, and the solid lines are calculated from models (Louca *et al.*, 1999).

shortcomings, the method of isotopic substitution is a powerful technique in identifying the local chemistry. A poor man's version is the chemical substitution method in which an element is replaced by another element with very similar chemical nature and different scattering lengths. The DDF of quasicrystalline Al–Mn was determined by replacing Mn with Cr that has a positive b and similar chemistry (Nanao *et al.*, 1987).

3.2.4. Joint Total and Differential PDF Studies

It is now possible to measure total PDFs with very high real-space resolution using high-energy X-rays or spallation neutrons. By the techniques mentioned above, it is also possible to measure DDFs. DDFs measured using anomalous X-ray diffraction are often of low real-space resolution because the energy of X-rays used is limited to the absorption edge of the atomic species in question. For transition metal oxides, this is generally below 10 keV; a severe limitation, though for a useful subset of elements in the fifth and sixth row of the periodic table, it is high enough to give good real-space resolutions. Even when the real-space resolution is low, the chemically resolved PDF contains useful complementary information to the high-resolution total PDF. It is also useful to combine two sets of PDFs determined by X-ray and neutron diffraction, since the partials are differently weighted. As we describe in Chapter 6, modeling programs exist which can simultaneously fit the same structural model to multiple datasets, including total and differential PDFs. There is likely to be a lot more of this kind of study in the future where the high real-space resolution measurement and the low resolution but chemically resolved PDFs put additional constraints on the modeling making the resulting structural solution more unique.

3.3. MAGNETIC CORRELATION FUNCTIONS

3.3.1. Magnetic Scattering of Neutrons

Neutrons are spin-1/2 particles. The spin of the neutron interacts with electron spins that give rise to magnetism in materials. Neutron scattering can be used to determine the spin configurations and magnetic structures of the material. In general, the scattering intensity from magnetic scattering is complicated because of its vector nature; the intensity depends on the dot product of the electron spin and the scattering vector \mathbf{Q} . We will not get into the details of physics of magnetic scattering and delegate it to standard textbooks (e.g., Lovesey, 1984), but we should note that the intensity of scattering of spin-polarized neutrons from a magnetic material has three parts, representing magnetic (spin–spin), spin–nucleus, and nuclear (nucleus–nucleus) interference functions;

$$I_{\text{total}} = I_{\text{M}} + I_{\text{S-N}} + I_{\text{N}} \quad (3.65)$$

Spin-polarized neutron beams can be created, usually by using Bragg diffraction from a magnetic crystal such as a Heusler alloy, or reflection from multilayered magnetic films, and most recently by sending the beam through spin-polarized ^3He . If a similar magnetic crystal is used as an analyzer, one can measure the intensity of scattered neutrons with the same spin as the incoming beam (spin non-flip) or opposite (spin flip). These two measurements can be done with the neutron spins either parallel or perpendicular to the scattering vector, \mathbf{Q} , that is, the polarization of the incoming beam lies either in the scattering plane or perpendicular to it. By combining these four sets of data, the three terms in Eq. (3.65) can be sorted out.

A less unique but useful way of distinguishing nuclear scattering from magnetic scattering is to look at the Q -dependence of the scattering intensity. Magnetic scattering falls off quickly with increasing Q due to the magnetic form factor as we describe below. The magnetic scattering intensity, I_M , is related to the magnetic structure function, $S_M(Q)$,

$$I_M(Q) = f_M^2(Q) S_M(Q), \quad (3.66)$$

where $f_M(Q)$ is the magnetic form factor which is the Fourier transform of the spin density distribution function of an atom. For instance, in transition metals such as Fe, the radius of magnetic electrons (three dimensional) is about 0.5 \AA . This means that, at $Q = 3 \text{ \AA}^{-1}$, the value of $f_M(Q)/f_M(0)$ is about 0.5, and if $S(Q) = 1$ as in the paramagnetic state, $I_M(Q)/I_M(0)$ is about 0.25. In comparison, thermal diffuse scattering due to phonons increases as Q^2 , as shown in (Eq. 2.29). Thus, magnetic and phononic contributions can be separated by examining the dependence on Q .

3.3.2. Magnetic PDF

A direct Fourier transformation of $I_M(Q)$ by

$$\rho_M(r) = \frac{1}{2\pi^2 r} \int I_M(Qr) \sin(Qr) Q dQ \quad (3.67)$$

gives the spin-spin correlation function. This function has broad peaks as shown in Fig. 3.11, since the width of the peak is equal to two times the radius of the spin distribution function around each atom. By dividing $I_M(Q)$ by the magnetic form factor to obtain $S_M(Q)$ by Eq. (3.66), we can determine the atom-atom spin correlation function,

$$\rho_A^M(r) = \frac{1}{2\pi^2 r} \int S_M(Q) \sin(Qr) Q dQ, \quad (3.68)$$

which is more sharply defined, as shown in Fig. 3.12. The relation between $\rho_M(r)$ and $\rho_A^M(r)$ is similar to that between the Fourier transform of $I(Q)$ for X-ray diffraction which gives an electron-electron distribution function and $\rho_{\text{og}}(r)$ which is an atomic correlation function.

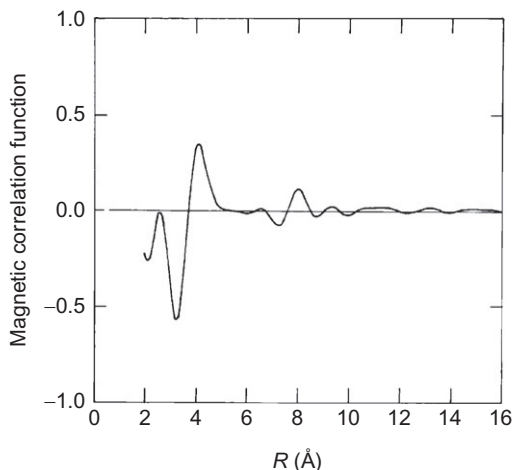


FIGURE 3.11 Magnetic PDF of amorphous Mn–Ni obtained by the direct Fourier transformation of magnetic intensity, $I_M(Q)$, determined by spin-polarized neutron diffraction (Wu *et al.*, 1987).

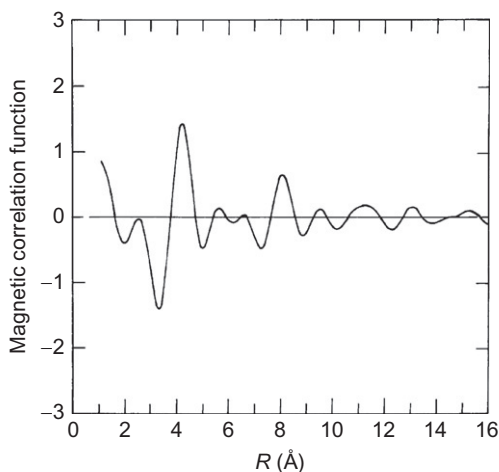


FIGURE 3.12 Atomically resolved magnetic PDF of amorphous Mn–Ni obtained by dividing $I_M(Q)$ by the magnetic form factor to obtain $S_M(Q)$ before Fourier transformation (Wu *et al.*, 1987).

As is well known, nickel is magnetic. Why, then, is the magnetic contribution invisible in the PDF, shown in Fig. 3.2? The answer is that the magnetic correlation peaks are wide and low, and completely buried under the nuclear peaks. For instance, since the radius of the three-dimensional electron cloud in Ni is $\langle r \rangle = 0.5 \text{ Å}$, the full width of the magnetic PDF is $22\langle r \rangle = 1.4 \text{ Å}$, which is 10 times the peak width for the nuclear PDF. The magnetic scattering length is 0.27 fm for 1 Bohr magneton, and thus for Ni, it is about 0.16 fm. The nuclear

scattering length, on the other hand, is $b_{\text{Nuclear}} = 1 \text{ fm}$, so $[b_{\text{Magnetic}}/b_{\text{Nucleus}}]^2 = 0.026$. Hence, the magnetic peak intensity will be only 2.6% of the nuclear peak intensity, which is negligible in Fig. 3.2. While this is a rather extreme case since the magnetic moment of Ni is small and nuclear scattering length is large, in general, magnetic correlation is not detectable from the PDF which is dominated by nuclear scattering. Spin-polarized neutron scattering measurements are necessary to determine the magnetic PDF.

3.4. THE PDF IN HIGHER DIMENSIONS

When the PDF technique is mentioned, it is usually assumed to apply to isotropic samples. In this case, the data are averaged over all directions in three-dimensional space resulting in a one-dimensional function, $g(r)$. However, there can be a case where the averaging takes place only over two dimensions rather than three dimensions. In this case, the scattering data are isotropically averaged in a single, well-defined, scattering plane in reciprocal space. These data can then be transformed to real-space coordinates resulting in a two-dimensional function $g(r, Q_n)$. In this case, \mathbf{Q}_n is a vector normal to this scattering plane and Q_n is the distance along \mathbf{Q}_n from the origin to the scattering plane of interest. This is known as the two-dimensional PDF. It is appropriate for studying samples with particular two-dimensional geometries, for example, thin films and multilayers, though to date its only application has been in a cylindrical geometry quasicrystal (He *et al.*, 1993). This is destined to change with the advent of third-generation synchrotron sources.

A related subject is that of surface scattering and surface correlation functions. In this case, a two-dimensional average of the scattering is taken; however, because the scattering is from a two-dimensional object, there is no structure in the scattering along the direction in Q -space perpendicular to the scattering plane: the scattering appears as structureless diffuse rods parallel to \mathbf{Q}_n . What results is a one-dimensional correlation function, the surface correlation function.

It is also possible to measure the entire reciprocal space of a single crystal, $S(\mathbf{Q})$, and transform the data to real space using a vector transform. The resulting function is a three-dimensional PDF, $g(\mathbf{r})$. Finally, we also note that lower dimensional correlation functions distinct from those mentioned above can be obtained by determining $S(\mathbf{Q})$ from a single crystal along specific directions in Q -space, \mathbf{Q}_z , and Fourier transforming this information. This results in a layer–layer correlation function, $g_{\text{layer}}(z)$, where the information in the real-space layer perpendicular to the \mathbf{Q}_z vector has been averaged. All these correlation functions are defined below.

3.4.1. PDF Defined in Three Dimensions

Let us go back to the definition of the PDF in Section 3.1. Since we live in the three-dimensional world, both the scattering vector \mathbf{Q} and the real-space vector \mathbf{r} are three dimensional. Only by taking the spherical average, representing

the powder average, did we arrive at the standard expression for the powder PDF (Section 3.1.2.1). If we do not take such averaging, the PDF is a three-dimensional function, given by

$$\rho_0[g(\mathbf{r}) - 1] = \frac{1}{8\pi^3} \int [S(\mathbf{Q}) - 1] \exp(-i\mathbf{Q} \cdot \mathbf{r}) d\mathbf{Q} \quad (3.69)$$

where $S(\mathbf{Q})$ is the structure function determined in the three-dimensional Q -space, and $g(\mathbf{r})$ is the three-dimensional density correlation function,

$$g(\mathbf{r}) = \frac{1}{\rho_0^2 V} \int \rho(\mathbf{r}') \rho(\mathbf{r}' + \mathbf{r}) d\mathbf{r}'. \quad (3.70)$$

Here, V is the sample volume and $\rho(\mathbf{r})$ is the single-atom density function. The trouble is that in order to obtain this function, the structure function $S(\mathbf{Q})$ has to be determined in continuous three-dimensional Q -space, and this is not an easy task. For instance, if we use a relatively coarse resolution of $\Delta Q = 0.01 \text{ \AA}^{-1}$, in order to scan the entire three-dimensional Q -space of $\pm 40 \text{ \AA}^{-1}$, scattering data have to be collected at as many as 5.12×10^{11} points. This is not impossible with the aid of a two-dimensional area detector, but it requires a long measurement time and a very large memory space (500 GB). To date, such a feat has never been accomplished, while an attempt on a smaller scale is under preparation. In addition, there are many complications in this type of measurement as we discuss below. While theoretically measuring the three-dimensional PDF may be the best approach to solve the problem of complex crystal structure, in practice, there are many alternatives that can be even better than the brute force three-dimensional measurement.

3.4.2. Anisotropic PDF

If the three dimensionality of the PDF is weak and the PDF is nearly spherically symmetric (isotropic), an expansion by the spherical harmonics is the easiest way to describe the anisotropy. We use a polar coordinate and expand $S(\mathbf{Q})$ and the PDF into radial and angular functions,

$$\begin{aligned} S(\mathbf{Q}) &= \sum_{\ell, m} S_{\ell}^m(Q) Y_{\ell}^m \left(\frac{\mathbf{Q}}{Q} \right), \\ g(\mathbf{r}) &= \sum_{\ell, m} g_{\ell}^m(r) Y_{\ell}^m \left(\frac{\mathbf{r}}{r} \right), \end{aligned} \quad (3.71)$$

where $Y_{\ell}^m(\mathbf{a})$ are the spherical harmonics. They are connected by

$$g_{\ell}^m(r) = \frac{i^{\ell}}{2\pi^2 \rho_0} \int S_{\ell}^m(Q) J_{\ell}(Qr) Q^2 dQ, \quad (3.72)$$

$$S_{\ell}^m(r) = \frac{i^{\ell}}{2\pi^2\rho_0} \int g_{\ell}^m(Q) J_{\ell}(Qr) Q^2 dQ, \quad (3.73)$$

where $J_{\ell}(x)$ is the ℓ th order spherical Bessel function. Note that $\ell=0$ corresponds to the powder PDF, Eq. (3.4), since $J_0(x) = \sin x/x$. Further details of this technique are given in Appendix 3.4, and some results for metallic glasses are given in Chapter 12.

3.4.3. One-Dimensional PDF and Layer–Layer Correlations

Quite often, it is mistakenly assumed that if a one-dimensional scan of the single crystal scattering data is Fourier transformed, it produces the atomic PDF along that direction. The fact is that if one collects the scattering intensity from a single crystal along Q_z including the diffuse scattering and applies the Fourier transform, what is produced by such a procedure is not the atomic PDF but the atomic layer–layer correlation function,

$$g_{\text{layer}}(z) = \frac{1}{L} \int \rho_2(z') \rho_2(z' + z) dz', \quad (3.74)$$

where z is parallel to \mathbf{Q} , L is the length of the sample in the z -direction, and $\rho_2(z)$ is the layer-averaged single-atom density function,

$$\rho_2(z) = \frac{1}{A} \int \rho(r) dx dy, \quad (3.75)$$

where A is the area of the sample in x – y plane. The layer–layer correlation function (3.74) is often confused with the one-dimensional correlation function averaged over the entire sample,

$$g_{1-d}(z) = \frac{1}{\rho_0^2 V} \int \rho(\mathbf{r}') \rho(\mathbf{r}' + \mathbf{z}) d\mathbf{r}'. \quad (3.76)$$

Note that in this case, the correlation function is volume averaged, while in Eqs. (3.74) and (3.75), the density function is averaged first, before evaluating the correlation function. In order to obtain the one-dimensional correlation function (3.76), one has to carry out an integration of $S(\mathbf{Q})$ over $Q_x - Q_y$ space,

$$S_z(Q_z) = \frac{1}{A_Q} \iint S(\mathbf{Q}) dQ_x dQ_y, \quad (3.77)$$

where A_Q is the area in the $Q_x - Q_y$ space over which the integration is carried out, and then apply the Fourier transform,

$$g_{1-d}(z) = \frac{1}{8\pi^3 L} \int [S_z(Q_z) - 1] \exp(-iQ_z z) dQ_z. \quad (3.78)$$

Thus, $S(\mathbf{Q})$ has to be determined over the entire three-dimensional space before this analysis can be carried out. There is no easy short cut in producing a three-dimensional PDF.

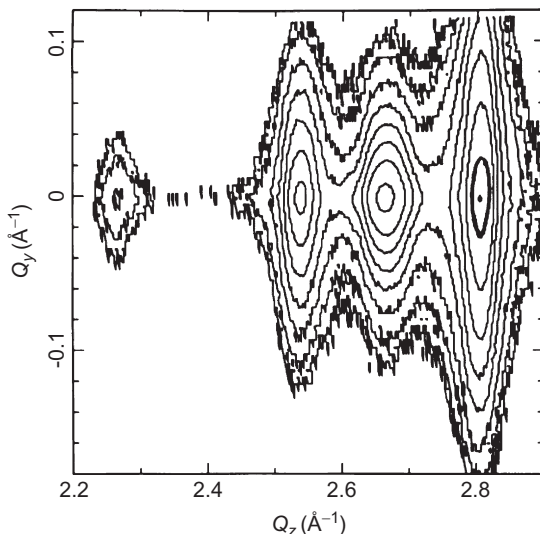


FIGURE 3.13 Scattering intensity from a Pt/Co multilayered film as a function of Q_z , normal to the surface and Q_y , parallel to the surface showing off-specular (i.e., $Q_y \neq 0$) diffuse scattering (Yan *et al.*, 1992).

The layer-layer correlation is useful in some cases. For instance, this procedure has been applied to multilayered films to determine their interfacial roughness. By measuring the specular reflectivity of the film with the \mathbf{Q} -vector along the normal of the surface, the roughness of the interface can be evaluated through Eq. (3.74). It should be noted, however, the concept of length scale of roughness is absent from this expression. Roughness can be of the atomistic level, originating from atomic diffusion, or of mesoscopic scale coming from the imperfect surfaces such as steps in the vicinal surface. These two can be separated if one measures the diffuse scattering in the off-specular directions, as shown in Fig. 3.13. By integrating the intensity in the $Q_x - Q_y$ plane, one obtains the one-dimensional correlation function (3.76), instead of the interlayer correlation function (3.74) (Yan and Egami, 1993). In the case of the Pt/Co multilayered films with the $\langle 111 \rangle$ orientation, the total thickness of the interface determined from the specular reflectivity is 8.7 Å, while the true local thickness due to diffusion is 6.9 Å. The difference is due to the mesoscopic correlated roughness.

3.4.4. Two-Dimensional PDF and Intralayer Correlation

If the data such as those in Fig. 3.13 are averaged over the angle in the plane retaining the radial Q length $Q_r = \sqrt{Q_x^2 + Q_y^2}$,

$$S_2(Q_r, Q_z) = \frac{1}{2\pi Q_r} \int S(\mathbf{Q}) d\varphi, \quad (3.79)$$

where φ is the angle in the $Q_x - Q_y$ plane, the Fourier transform of this function is the in-plane two-dimensional PDF,

$$\rho_0 g(R, Q_z) = \frac{1}{2\pi} \int [S_2(Q_r, Q_z) - 1] J_0(Q_r r) Q_r dQ_r, \quad (3.80)$$

where $J_0(Q_r, Q_z)$ is the zeroth order spherical Bessel function. By applying Eq. (3.80) on the off-specular diffuse scattering in Fig. 3.13, one obtains the autocorrelation function for the film roughness as Fig. 3.14 (Yan *et al.*, 1992). It gives the interfacial height–height correlation function similar to the surface height–height correlation function (Sinha *et al.*, 1988).

This method was also applied on a decagonal quasicrystal $\text{Al}_{65}\text{Cu}_{15}\text{Co}_{20}$ which is quasiperiodic in the x – y directions but is periodic in the z -direction (He *et al.*, 1993). The averaging over the planar angle can easily be done by rotating the sample around an axis (z -axis) during the measurement. By using the PDF resolved for ℓ , the in-plane atomic structure of this compound was analyzed. The results are shown in Figs. 3.15 and 3.16. This technique can also be applied to the PDF of a surface.

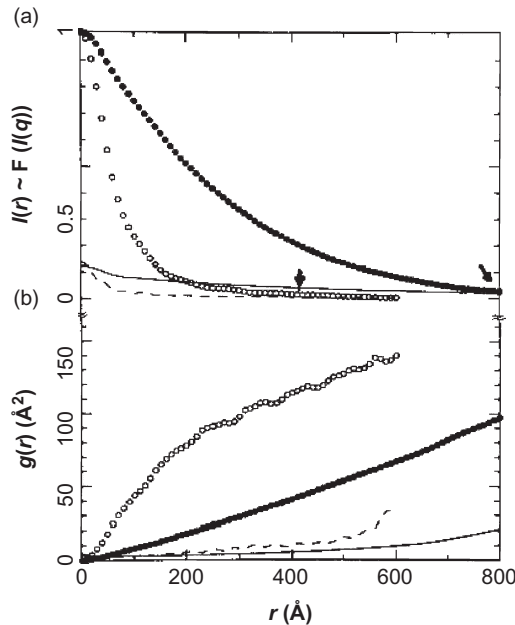


FIGURE 3.14 Roughness autocorrelation function obtained by Fourier transforming the diffuse scattering in Fig. 3.13 (Yan and Egami, 1993).

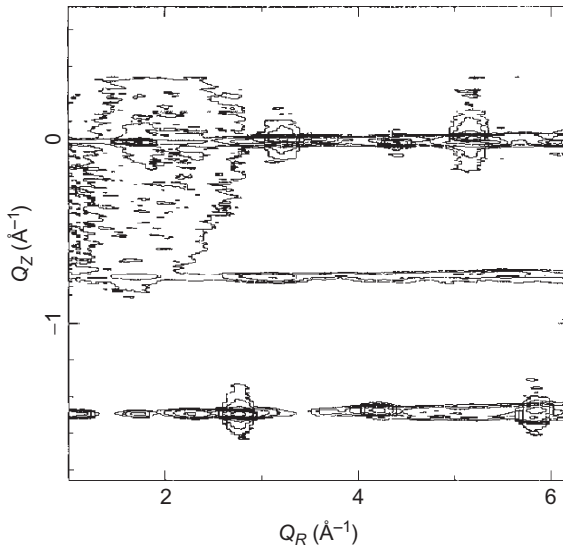


FIGURE 3.15 Two-dimensional intensity contour plot of scattering from a decagonal quasicrystal $\text{Al}_{65}\text{Cu}_{15}\text{Co}_{20}$. The sample was rotated about the z -axis during the experiment resulting in the intensity being averaged over h - and k -directions. This intensity is plotted as Q_R at different values of Q_z (He *et al.*, 1993).

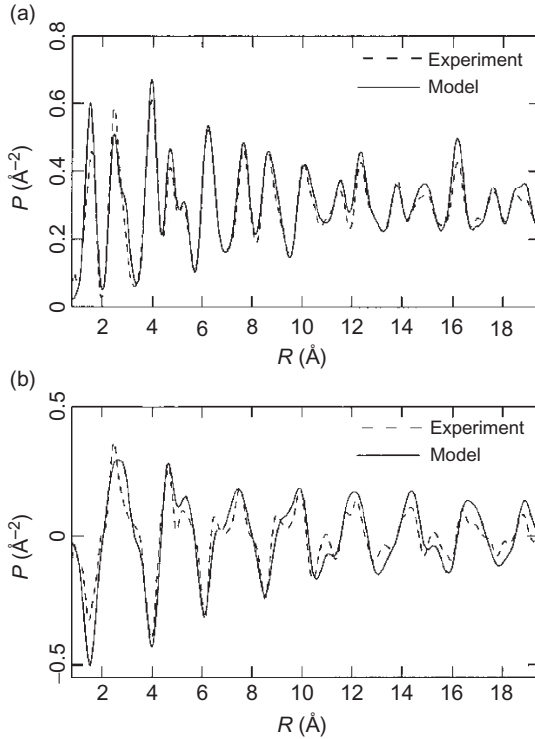


FIGURE 3.16 PDFs obtained from the data in Fig. 3.15. The PDFs shown result from Fourier transforming data from $Q_z=0$ (a) and $Q_z=1.52 \text{ \AA} = 2\pi/c$ (b). The dashed lines are from models (He *et al.*, 1993).

3.4.5. Three-Dimensional PDF and the Powder PDF

As we discussed above, theoretically the best way to determine the three-dimensional structure is to collect the diffraction data in three dimensions and obtain the three-dimensional PDF. However, such a measurement is very time consuming, and also a single crystal may not be always available, particularly when we are studying new materials. Furthermore, there are many technical complications associated with this method. First is the dynamic range of the measurement. The intensity of the Bragg peak is much stronger than the diffuse scattering by many orders of magnitude. The ratio depends upon the resolution, but a difference by five to seven orders of magnitude is not rare. The detector has to be able to accommodate such a wide dynamic range, without saturation at high count rates and without background electrical noise at low-count rates. Then, in order to measure the diffuse scattering accurately, the background scattering has to be very low. The spectrometer has to be specially designed to reduce the background scattering. In addition, for large crystals, the extinction and multiple scattering of the Bragg peaks presents a major problem. It is relatively easy to carry out a qualitative, or semiquantitative, measurement of $S(\mathbf{Q})$ over three dimensions. It is very difficult to determine $S(\mathbf{Q})$ with the precision required to obtain an accurate PDF.

Thus, the PDF is usually reduced to one dimension by making the measurement on a powder sample. By taking the orientational averaging, we lose the angular information. This might appear as a very severe compromise, and one might argue that an accurate three-dimensional single crystal study of the Bragg peaks coupled with a measurement of the diffuse scattering over a limited Q -space as is usually done is still better than the PDF study when some disorder is present. However, the argument is not so simple. First, the merit of collecting all the diffuse scattering in the powder scattering should not be underestimated. Unless one has a very good idea where the diffuse scattering occurs in the three-dimensional Q -space, one may miss important information in the study of diffuse scattering from a single crystal. The merit of being able to collect all the diffuse scattering by the powder measurement often outweighs the disadvantage of losing angular information.

3.5. ERROR ANALYSIS FOR THE PDF

3.5.1. Error Diagnostics

Let us assume that you finally obtained a PDF, by the methods explained in the next two chapters. How do you know if the results are correct? For instance, if a small, unexpected peak was found in your PDF, how do you know if that peak is real, or just some noise? Particularly, if this peak fits to your theory or expectations, how do you know that you are not fooling yourself? A short answer is that you do not know. However, features of typical errors are well known so that by elimination you can reduce the chance of making a mistake. The most

conspicuous errors are ripples at short distances. It is physically impossible for atoms to come too close to each other so that $g(r)$ has to be equal to zero below a certain distance. In reality, however, $G(r)$ oscillates around zero as shown in Fig. 3.5, for example. In the following, we discuss where these oscillations come from and how to reduce them.

3.5.2. Termination and Normalization Errors

As discussed in Section 3.1.4, terminating the integration in Eq. (3.4) results in spurious oscillation in the data, known as termination ripples or errors. In Appendix 3.2, this effect was shown to be given by

$$G'(r) = \frac{1}{\pi} \int_0^\infty G(r') \left[\frac{\sin Q_{\max}(r-r')}{r-r'} - \frac{\sin Q_{\max}(r+r')}{r+r'} \right] dr', \quad (3.81)$$

where $G(r)$ is the true reduced pair density function. The convoluting function defined by Eq. (3.81) is shown in Fig. 3.17. If the PDF has a peak given by a δ -function, the measurement yields a peak with many satellites given by Eq. (3.81). Fortunately, the PDF is not composed of δ -function peaks, but of wider Gaussian-like peaks because of the atomic vibrations. Figure 3.18 shows how the original shape of the PDF peak is restored as the value of Q_{\max} is increased. In general, if the value of Q_{\max} is greater than $3/\langle u^2 \rangle^{1/2}$, the effect of termination is negligible (Toby and Egami, 1992). It is useful to consider this problem in Q -space. The nonzero width of the PDF peak gives rise to the Debye–Waller factor as discussed in Chapter 2. Because of this effect, $S(Q)$

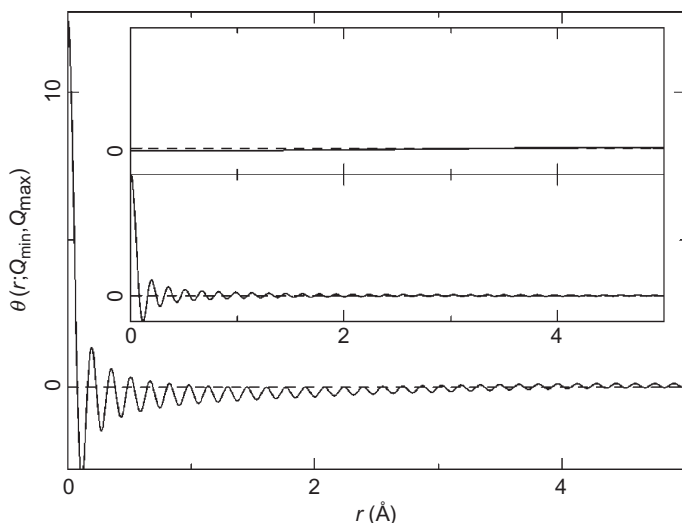


FIGURE 3.17 PDF termination function plotted for the case of $Q_{\min}=0.9 \text{ \AA}^{-1}$ and $Q_{\max}=40 \text{ \AA}^{-1}$ (Peterson *et al.*, 2003).

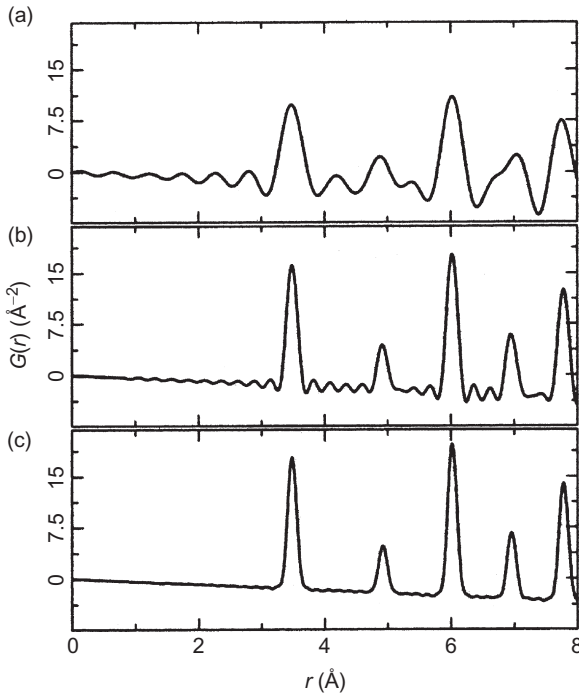


FIGURE 3.18 Calculated PDF of lead assuming $\langle u^2 \rangle = 0.0025 \text{ \AA}^{-2}$ comparable to that expected at low temperature. The calculated PDF has then been convoluted with the termination function (Eq. 3.81) assuming a Q_{max} of (a) 12, (b) 24, and (c) 36 \AA^{-1} . Because of the DW effects giving finite width Gaussian PDF peaks, the ripples have almost gone by $Q_{\text{max}} = 36 \text{ \AA}^{-1}$. This highlights the fact that accurate PDFs can be obtained if data are collected to sufficiently high Q_{max} without resorting to artificially damping the data.

approaches unity. That means the value of $S(Q) - 1$ becomes smaller with increasing Q , and if it is small enough at Q_{max} , the effect of termination is minimal. If Q_{max} is roughly equal to $3/\langle u^2 \rangle^{1/2}$ the Debye–Waller factor is about 0.03, which is usually small enough.

As we just mentioned, ideally $S(Q)$ converges to unity at large Q values. However, if the data are not normalized well enough, $S(Q) - 1$ will have a step at the termination at Q_{max} and produces strong ripples in $G(r)$, that is, a normalization error produces termination errors even when the true structure function converges to unity before Q_{max} . This is explored in more detail by Peterson *et al.* (2003).

3.5.3. Statistical Errors

In order to eliminate the termination errors, a high enough value of Q_{max} should be chosen. However, extending the range of Q increases the chances of including noise due to statistical errors. These are roughly proportional to $S(Q)/N$, where N is the detector count. Since, in Eq. (3.4), the integral includes the

multiplication by Q , the damage due to noise increases with Q . The error in $S(Q)$, $\Delta S(Q)$, affects the PDF through (Toby and Egami, 1992),

$$\rho_0^2 \Delta g(r)^2 = \frac{1}{4\pi^4 r^2} \sum_v [\Delta S(Q_v) Q_v dQ_v \sin(Q_v r)]^2, \quad (3.82)$$

where v enumerates data points, and dQ_v is the Q -spacing between the data points. The derivation of Eq. (3.82) is discussed in Appendix 5.3 in more detail. If the noise is purely due to statistics, this can be approximated as

$$\rho_0 \Delta g(r) = \frac{1}{2\sqrt{2}\pi^2 r} \left[\int \frac{Q_2 dQ}{I(Q)} \right]^{1/2}, \quad (3.83)$$

where $I(Q) = N(Q)/dQ$, $N(Q)$ being the detector count. These results tell us a couple of points regarding the statistical noise:

The noise in $g(r)$ decreases with r as $1/r$ and is constant with r in $G(r)$.

The noise is cumulative; extending the Q range always increases noise.

Thus it is important to determine where to terminate $S(Q)$, by balancing termination error and noise.

3.5.4. Effect of Q -Resolution

The effect of Q -resolution is different for the diffraction measurement with a monochromatic beam, such as high-energy X-ray scattering, and for the pulsed neutron tof measurement. In the case of the monochromatic beam, the Q -resolution, ΔQ , is nearly constant in Q , while for the tof measurement, it is approximately proportional to Q . Interestingly, the mathematics involved in the analysis of the effect of Q -resolution is an exact inverse of the effect of atomic vibration discussed in Section 2.1.3. If the resolution is independent of Q , the effect of Q -resolution can be expressed as a convolution of the true scattering intensity, $I_t(Q)$, by the resolution function, $\Phi(Q)$

$$I(Q) = \int I_t(Q - Q') \Phi(Q') dQ'. \quad (3.84)$$

Thus, the Fourier transform is the product of the Fourier transform of each, according to the convolution theorem,

$$g(r) = g_t(r) \Gamma(r), \quad (3.85)$$

where $\Gamma(r)$ is the Fourier transform of the resolution function. Thus, if the resolution function is Gaussian, the Fourier transform is a Gaussian function as well, with the standard deviation given by $1/\sigma_Q$, where σ_Q is the standard deviation of the resolution function, in analogy of the Debye–Waller factor. Thus, the effect is not felt until r is large enough ($> 2\pi/\Delta Q$).

However, in the case of the tof measurement, the resolution is approximately proportional to Q . Thus, the convolution theorem cannot be used in

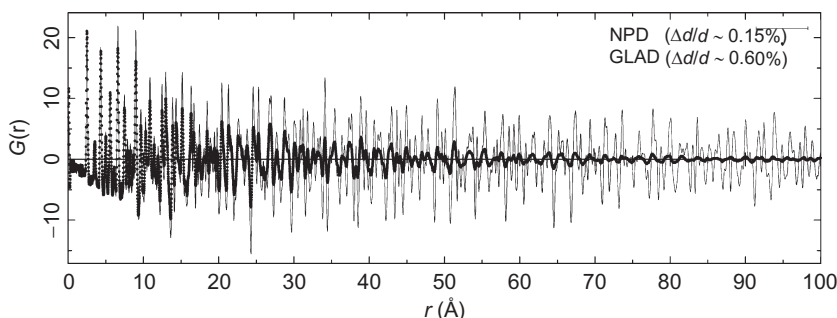


FIGURE 3.19 Effect of Q -resolution on the PDF. (a) Data are nickel powder measured at GLAD at IPNS (low-resolution diffractometer, $\Delta d/d \sim 0.6\%$) and NPD at the Lujan Center (high-resolution diffractometer, $\Delta d/d \sim 0.15\%$). The resulting PDFs are shown plotted on top of each other all the way to 100 Å. The loss of information in the nanometer range in the low-resolution measurement is clearly apparent.

this case. Since the details of the PDF are determined by the high- Q portion of the data, the worsening resolution at high- Q is problematic. In Fig. 3.19, the effect of Q -resolution in this case is illustrated. For $\sigma_Q = 0.006$ the PDF becomes less defined even at 10 Å, and in the medium-range distance of 10–20 Å, the effect is quite visible. Thus, in order to determine the PDF over a large distance range, it is important to use a high- Q -resolution, even at the expense of intensity.

3.5.5. Effect of Other Systematic Errors

As we will discuss later, inaccuracies in various data processing procedures, such as absorption correction, contribute to systematic errors. They typically affect the data in the form of (Peterson *et al.*, 2003)

$$S_{\text{obs}}(Q) = A(Q)S_{\text{true}}(Q) + B(Q). \quad (3.86)$$

As we discuss below, inaccuracies in absorption correction are represented by $A(Q)$, while inaccuracies in the multiple-scattering correction and inadequate background correction are included in $B(Q)$. The effect of $A(Q)$ can be described by a convolution. Usually, $A(Q)$ is a slowly varying function of Q , and consequently, its Fourier transform resembles the termination function (3.81). Thus, if the characteristic Q values that represent the periodicity of $A(Q)$ are Q_E , ripples appear at $7.8/Q_E$. As for the effect of $B(Q)$, clearly its Fourier transform adds to the PDF. Again $B(Q)$ usually varies slowly with Q , and the effect in the PDF decreases quickly with r . In the distance range of interest, the effect is usually small. That is why the PDF is remarkably reliable, even though it is impossible to eliminate all the errors in $S(Q)$ (Peterson *et al.*, 2003).

3.5.6. Remedies of Errors

Various methods have been proposed to reduce the effects of termination error and other errors. Historically, the most commonly used method to combat the termination error is to use a damping function for the window function in Eq. (A3.3.1) so that $S(Q) - 1$ converges smoothly to zero. For instance, a Gaussian function

$$W(Q) = e^{-BQ^2} \quad (3.87)$$

is frequently used. Its effect is to add to the Debye–Waller factor and make the PDF peak wider than it really is.

Another approach is to extend $S(Q)$ artificially beyond the range over which it is actually experimentally determined so that obvious errors are reduced. One possibility is to force $g(r) = 0$ below a certain cutoff distance and extend $S(Q)$ either using an iterative method or using the maximum entropy method. The use of the maximum entropy method is an attractive, but potentially dangerous, approach. While beautiful PDFs without oscillations can be obtained by this method, the uniqueness of the result is lost, since the result is strongly dependent upon the details of the constraint. For instance, depending upon the range in r over which $g(r) = 0$ is enforced, the PDF peak height changes by a large amount. This is discussed further in Chapter 6. Generally, nothing is better than actually collecting the data accurately up to high values of Q . Other corrections are largely cosmetic and would not help recovering useful information. One of the reasons why they are cosmetic is that the PDF is obtained by the Fourier transformation, which already is an excellent noise screening method.

3.6. INFORMATION CONTENT IN THE PDF AND THE NYQUIST–SHANNON SAMPLING THEOREM

The PDF is the Fourier transform of the diffraction data. The issue of understanding the propagation of information through a Fourier transform such as this was first discussed by Shannon (1949) in the context of communications and signal processing. It is a well-known theorem but bears repeating and being applied explicitly to the PDF equations (Farrow *et al.*, 2011). Simply put, the Nyquist–Shannon (NS) sampling theorem states “If a function $\chi(t)$ contains no frequencies higher than B hertz, it is completely determined by giving its ordinates at a series of points spaced $1/(2B)$ seconds apart” Shannon (1949). It is conventional in the PDF literature to specify an arbitrary grid for the PDF that makes the function look smooth. This is often 0.01 Å. There is no harm in doing this, but plotting the function on a grid finer than that specified by the NS theorem does not add any additional information to the PDF. Oversampling the grid in real space does have the downside both of slowing down modeling programs since they have to calculate the PDF on unnecessary points and also making uncertainty correlations between points greater and

leading to larger underestimates of the uncertainties on refined parameters from modeling programs (when indeed they do estimate the uncertainties at all) (Chapter 6).

In the context of PDF, the frequency spoken about by Shannon is Q and we are interested in sampling in r space, the analog of the time domain. The frequency information is specified by $F(Q)$, which has a bandwidth Q_{\max} . This gives a Nyquist interval of (Farrow *et al.*, 2011)

$$dr_N = \frac{\pi}{Q_{\max}}. \quad (3.88)$$

The sampling theorem states that the PDF can be sampled on any grid with intervals smaller than this without losing any information from $F(Q)$. If data are sampled on a grid courser than this, then information is lost from $F(Q)$. The information loss happens in a particular way through aliasing, which is described in some detail in Farrow *et al.* (2011) as it applies to the PDF.

The sampling theorem determines the number of data points required to reconstruct a PDF signal from materials as

$$N \approx \frac{\Delta r}{dr_N} - 1 = \frac{\Delta r Q_{\max}}{\pi} - 1, \quad (3.89)$$

where Δr is the range of r over which the PDF is determined. What is more relevant to PDF modeling is the *number of pieces of structural information* in the PDF. N is an upper bound on this, since we cannot extract more independent observations of the structure than raw information from the signal. Given perfect data and the proper model, one can meaningfully extract N structural parameters from a PDF signal. In general, it is possible to extract fewer structural parameters due to a number of reasons, and taking a lead from the Rietveld refinement literature, this factor may be $N/3 - N/5$ (McCusker *et al.*, 1999). Factors such as noise and peak overlap can obscure the structural information in the PDF. For example, consider a situation where the range of the PDF being fit contains only a single peak, but was measured with a very large Q_{\max} , yielding a large value for N . In this case, a complete structure model cannot be obtained from fitting this single peak, no matter how large N is, because the relevant structural information is not in the data. More peaks are needed, not more independent points on the same peak. In another extreme case, imagine that there are many PDF peaks but the majority of them have a single point or no points due to a small Q_{\max} . In this situation, the position and shape of the peaks cannot be determined. In practice, as we discuss in Chapter 6, the amount of structural information in the PDF cannot be precisely known but N is a hard upper bound.

If the PDF analysis is applied on a perfectly crystalline solid, different portions of the PDF reflect the same structure, so they share the same information and are correlated to each other. In this case, the amount of information the PDF contains is much less than N . On the other hand, if the solid is imperfect

and each crystallographic unit cell is slightly different from each other, for instance due to defects, different regions of the PDF carry *different* information. In this case, N may be closer to the real number of pieces of structural information. This just illustrates an obvious point that the PDF method is most powerful and meaningful when it is applied to disordered complex materials with local correlations.

A feature has been added to the PDFgui software to automatically resample the data onto the NS grid before fitting. Before having the confidence to use such a feature, it is interesting to test how well such a strategy works (Farrow *et al.*, 2011). In this study, neutron PDFs from Ni and LaMnO_3 were resampled onto different grids and fit using PDFgui. The refined parameters on the data with the finest grid, 0.01 \AA , were defined as the “correct” values. The values refined for coarser grids were then scored against the correct values using a “quality factor” that took the value 0 when the refined value was the same as the correct value and when it had the value 1 the refined value deviated from the correct value by 1 standard deviation. This was determined for each refined parameter in the fit. A plot of the refined parameter quality factors as a function of grid size is shown in Fig. 3.20, which also has representative plots of the PDFs from

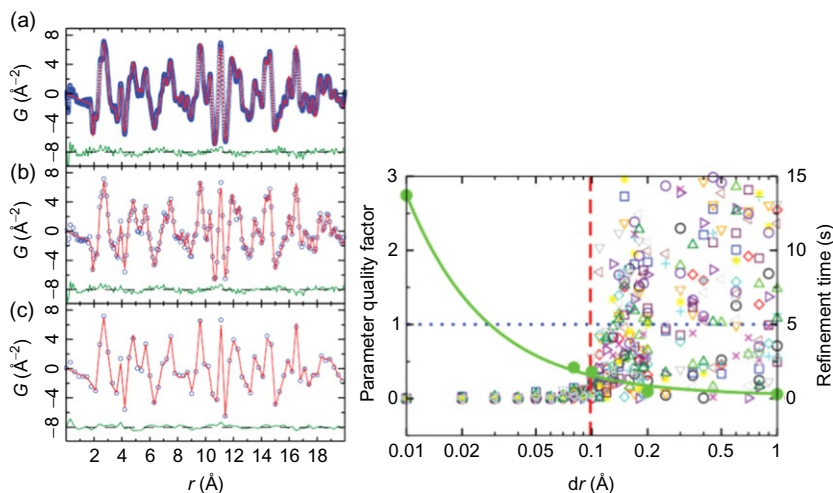


FIGURE 3.20 (Left) Neutron PDFs from the perovskite LaMnO_3 resampled onto different grids. (a) The default $0.01\text{-}\text{\AA}$ grid. The data in (b) are on a $0.1\text{-}\text{\AA}$ grid, which is close to the Nyquist–Shannon sampling frequency for these data. The data in (c) are undersampled, being on a grid of 0.3 \AA . The solid lines are PDFgui fits of the LaMnO_3 model to the data. In the right panel, a parameter quality factor is shown versus sampling grid size. This factor has a value 0 when the correct value of the parameter is refined (defined as the value refined on the 0.01 \AA grid) and a value 1 when the refined value is one standard deviation away from the correct value. The smooth curve is a plot of the computation time to calculate a PDF versus the grid spacing (Farrow *et al.*, 2011).

LaMnO₃ on three different grids. The results are quite remarkable. As expected, and given by the NS sampling theorem, parameters refined to PDFs on grids finer than the NS grid all yield quality factors close to zero, that is, the same model was obtained when the PDF was sampled on different grids without violating the sampling theorem. However, rather than the quality of the refined parameters gradually falling off as the grid is coarsened beyond dr_N , the parameters become quite unreliable almost immediately when the theorem is violated. The reason is not known, but presumably is related to instabilities in the refinement process in the presence of aliasing errors.

Also shown in the figure is the speedup in the computation time with grid size. In this case, there is an almost $8 \times$ speedup when refining the data on the NS grid rather than the default 0.01-Å grid, resulting in the same parameter values being refined. Refining on the NS grid also results in reduced error correlations between the points in the PDF (Xiaohao Yang, Pavol Juhas, Simon Billinge, unpublished) and therefore more accurate estimates of the refined parameter uncertainties. It is therefore recommended that modeling be carried out with PDFs on the NS sampling grid dr_N . As the plots of the data in Fig. 3.20 show, the PDFs are less esthetically pleasing when plotted on the NS grid than on the default 0.01 Å grid, but this is no more than esthetics. The theorem is clear that they contain absolutely no additional information!

APPENDIX 3.1. BEEVERS–LIPSON STRIPS

This account relies heavily on the excellent article “The Mechanism of Beavers–Lipson Strips” Gould (1998) and the account of Warren (1990) since the authors have never had the pleasure of actually using Beavers–Lipson strips ourselves!

To Fourier transform a quasicontinuous function like $S(\mathbf{Q})$, it involves a sum over every point in $S(\mathbf{Q})$ for each point in $G(r)$. With modern computers, we routinely utilize 1500 points in $S(\mathbf{Q})$ and compute 1000 points in $G(r)$ which requires the computer to make 10^6 calculations. This would clearly be a highly arduous task for the most ardent of graduate students, slide rule in hand. It became significantly easier in 1936 with the development of Beavers–Lipson strips.

The Beavers–Lipson strips were strips of cardboard which contained precomputed values of

$$A \sin \frac{2\pi h i}{120} \quad (\text{A3.1.1})$$

(there were also cosine strips containing $A \cos(2\pi h i/120)$). There was one strip for each value of A and h (4000 strips in all) and on the strip was printed 30 numbers which were the values of Eq. (A3.1.1) for $1 < i < 30$. Strips for integer values of h from 1 to 30 were available for each value of A . The values of A that were available were $-100 < A < 100$ in integer steps, then $-900 < A < 900$ in steps of 100.

Now, let us assume that we want to Fourier transform a measured $F(Q) = Q[S(Q) - 1]$ according to Eq. (3.4), reproduced here,

$$G(r) = \frac{2}{\pi} \int_0^\infty Q[S(Q) - 1] \sin(Qr) Q dQ. \quad (\text{A3.1.2})$$

This can be rewritten as

$$G(r_i) = \frac{2}{\pi} \sum_{h=1}^N Q_h [S_h - 1] \sin(Q_h r_i) \Delta Q. \quad (\text{A3.1.3})$$

The argument of Eq. (A3.1.1) can be written as $(4\pi h/60)(n/4)$. Thus, if we make the assignment $Q_h = (4\pi h/60)$ and $r_i = (i/4)$, we see that we can transform 30 Q -points in steps of $\sim 0.2 \text{ \AA}^{-1}$ up to $Q_{\max} \sim 6.2 \text{ \AA}^{-1}$. Furthermore, using the identity

$$A \sin \frac{2\pi h i}{120} = -(-1)^n A \sin \frac{2\pi(60-h)i}{120} \quad (\text{A3.1.4})$$

allows Q -points in the range of 30–60 to be evaluated (extending Q_{\max} to $\sim 13 \text{ \AA}^{-1}$) using the available strips. Then, we make the assignment $A_h = (2/\pi) Q_h [S_h - 1] \Delta Q$. To increase accuracy, it is necessary to work with A in the region of -100 to 100 , and so in practice, it would be scaled to bring the values into this range, the final PDF then being divided in turn by this same factor.

The evaluation would then go as follows. For each Q -point, the Beevers–Lipson strip corresponding to the right h and A value was selected from the box (Fig. 3.6) and placed on a large table. Each subsequent strip was placed below the previous one such that the columns of i -values lined up. The Fourier transform could then be evaluated at each i -point by summing the numbers on the strips in each i -column. The summation was either done using a mechanical calculator, or more commonly, using mental arithmetic. The assignment above allowed the PDF to be calculated up to 7.5 \AA in steps of 0.25 \AA . By using the identity A3.1.4 suitably modified so that h and i are interchanged, it is possible to extend the i -points in the range of 30–60 and r_{\max} to 15 \AA .

As Warren (1990) points out “The whole procedure is very simple and it is readily performed in 3 or 4 h.” Nonetheless, the use of an electronic computer is definitely to be preferred: as Gould (1998) mentions “Today, ... Fourier transforms on several thousand data items... require less time than it takes to gulp down a cup of coffee.” The Beevers–Lipson strips approach may be healthier, but certainly more arduous and prone to error! Other historical gems from the Gould (1998) article include the fact that 500 boxes of Beevers–Lipson strips were sold between 1948 and 1970 and the big stir caused by the publication, in a crystallography newsletter of the British Crystallography Association, of a picture of Arnold Beevers and Henry Lipson in swimming costumes entitled “Beevers and Lipson stripped.”

APPENDIX 3.2. TERMINATION ERROR

When the Fourier transformation in Eq. (3.4) is terminated at Q_{\max} , the result can be rewritten as

$$\begin{aligned} G'(r) &= 4\pi r \rho_0 [g'(r) - 1] = \frac{2}{\pi} \int_0^{Q_{\max}} [S(Q) - 1] \sin(Qr) Q dQ, \\ &= \frac{2}{\pi} \int_0^{\infty} W(Q) [S(Q) - 1] \sin(Qr) Q dQ, \end{aligned} \quad (\text{A3.2.1})$$

where $W(Q)$ is the window function,

$$W(Q) = 1 (Q \leq Q_{\max}) = 0 (Q > Q_{\max}). \quad (\text{A3.2.2})$$

In mathematics, it is well known that the Fourier transform of a product A and B , $F\{AB\}$, is a convolution of the transform of each, $F\{A\}$ and $F\{B\}$;

$$F\{AB\}(r) = \int F\{A\}(r') F\{B\}(r - r') dr'. \quad (\text{A3.2.3})$$

Since

$$\begin{aligned} \int F\{A\}(r') F\{B\}(r - r') dr' &= \frac{1}{(2\pi)^2} \iint A(Q') e^{iQ'r'} dQ' B(Q) e^{iQ(r-r')} dQ dr', \\ &= \frac{1}{(2\pi)^2} \iint A(Q') B(Q) e^{iQr} e^{i(Q'-Q)r'} dr' dQ' dQ, \\ &= \frac{1}{2\pi} \iint A(Q') B(Q) e^{iQr} \delta(Q' - Q) dQ' dQ, \\ &= \frac{1}{2\pi} \int A(Q) B(Q) e^{iQr} dQ = F\{AB\}(r). \end{aligned} \quad (\text{A3.2.4})$$

Now,

$$G'(r) = \frac{1}{i\pi} \int_0^{\infty} W(Q) [S(Q) - 1] (e^{iQr} - e^{-iQr}) Q dQ \quad (\text{A3.2.5})$$

then

$$G'(r) = \frac{1}{i\pi} \left[\int_0^{\infty} W(Q) [S(Q) - 1] e^{iQr} Q dQ + \int_{-\infty}^0 W(-Q) [S(-Q) - 1] e^{iQr} Q dQ \right]. \quad (\text{A3.2.6})$$

Since $S(-Q) = S(Q)$, if we define $W(Q)$ as,

$$W(Q) = 1 (-Q_{\max} < Q < Q_{\max}) = 0 (\text{otherwise}), \quad (\text{A3.2.7})$$

we obtain

$$G'(r) = \frac{1}{i\pi} \int_{-\infty}^{\infty} W(Q) [S(Q) - 1] e^{iQr} Q dQ = \int_{-\infty}^{\infty} w(r - r') G(r') dr', \quad (\text{A3.2.8})$$

where $G(r)$ is the ideal PDF,

$$\begin{aligned}
G(r) &= \frac{1}{i\pi} \int_{-\infty}^{\infty} [S(Q) - 1] e^{iQr} Q dQ, \\
&= \frac{1}{i\pi} \left[\int_0^{\infty} [S(Q) - 1] e^{iQr} Q dQ + \int_{-\infty}^0 [S(Q) - 1] e^{iQr} Q dQ \right], \\
&= \frac{1}{i\pi} \left[\int_0^{\infty} [S(Q) - 1] e^{iQr} Q dQ - \int_0^{\infty} [S(Q) - 1] e^{-iQr} Q dQ \right], \\
&= \frac{2}{\pi} \int_0^{\infty} [S(Q) - 1] \sin(Qr) Q dQ
\end{aligned} \tag{A3.2.9}$$

and $wt(r)$ is the Fourier transform of the window function,

$$wt(r) = \frac{1}{2} \int_{-Q_{\max}}^{Q_{\max}} e^{iQr} dQ = \frac{\sin(Q_{\max}r)}{r}. \tag{A3.2.10}$$

This function, shown in Fig. 3.17, has a large central peak and becomes a δ -function at the limit of infinite Q_{\max} . However, for finite values of Q_{\max} , it has side ripples that decay with distance. These ripples produce the termination errors. The first side peak is located at $r \sim 7.8/Q_{\max}$. Equation (A3.2.8) may be expressed as

$$\begin{aligned}
G'(r) &= \int_0^{\infty} wt(r-r') G(r') dr' + \int_{-\infty}^0 wt(r-r') G(r') dr', \\
&= \int_0^{\infty} [wt(r-r') - wt(r+r')] G(r') dr',
\end{aligned} \tag{A3.2.11}$$

or

$$G'(r) = \frac{1}{\pi} \int_0^{\infty} G(r') \left[\frac{\sin Q_{\max}(r-r')}{r-r'} - \frac{\sin Q_{\max}(r+r')}{r+r'} \right] dr'. \tag{A3.2.12}$$

APPENDIX 3.3. THE X-RAY ABSORPTION FINE STRUCTURE METHOD AND THE PDF METHOD

The X-ray absorption coefficient of a solid has many oscillations as a function of energy just above the absorption edge, which is called the X-ray absorption fine structure (EXAFS). This phenomenon has been known for a long time but was interpreted only in the 1970s in terms of the interference between the wavefunction of outgoing photoelectrons with that of photoelectrons backscattered by the near neighbors (Lytle *et al.*, 1975; Stern *et al.*, 1975). By analyzing these oscillations, the distance to the neighboring atoms can be determined. Since photoelectrons come out primarily from the element, of which absorption edge is just below the energy of the incident X-ray, the EXAFS provides the information

about the environment of a particular element. Details about the technique can be found in a recent general text (Koningsberger and Prins, 1988).

The X-ray absorption coefficient, $\mu(E)$, where E is the energy of X-ray, may be expressed in terms of the momentum of the outgoing photoelectron,

$$k = \frac{\sqrt{m(E - E_{\text{edge}})}}{\hbar}, \quad (\text{A3.3.1})$$

where m is the mass of an electron and E_{edge} is the absorption edge energy, as $\mu(k)$. By normalizing it against that of an isolated atom, $\mu_0(k)$, one obtains $X(k)$,

$$X(k) = \frac{\mu(k)}{\mu_0(k)} - 1. \quad (\text{A3.3.2})$$

Its Fourier transform

$$G(r) = \int e^{2ikr} X(k) k^n dk, \quad (\text{A3.3.3})$$

where $n=2$ or 3 , is called the PDF. Indeed, the position and intensity of the peaks of $|G(r)|$ roughly correspond to interatomic distances and coordination number. Also from the phase of $G(r)$, it is often possible to determine the chemical identity of the neighboring atoms.

However, because of many factors involved in scattering of electrons, $X(k)$ is modified in various ways. For instance, the PDF peak appears usually at a distance significantly shorter than the real distance due to the phase shifts. Also $X(k)$ can be strongly affected by multiple scattering, in particular if atoms are nearly linearly lined up. Furthermore, $X(k)$ is given as the sum of contributions from various neighbors,

$$X(k) = \sum_j \chi_j(k) e^{-2ikr_j}, \quad (\text{A3.3.4})$$

where r_j is the distance to the neighbor j , while the form factor, $\chi_j(k)$, depends strongly on j . This form factor describes the atomic potential that scatters electrons and the lifetime of photoelectrons, and its amplitude decreases rapidly with r_j . Thus, the Fourier transform of $X(k)$ is not exactly the pair density function (PDF). As shown in Fig. A3.3.1 as an example, $G(r)$ is significantly different from the PDF both in the peak shape and in the intensity. Thus, the experimental data themselves do not directly provide the structural information, and the structure is determined only through calculating $X(k)$ and its Fourier transform for a particular model. The problem is that the theoretical $X(k)$ depends upon the method of calculation, and there is no unique way of calculating it. This lack of uniqueness is the greatest weakness of the EXAFS method. Even though the EXAFS method is easy to implement, it is dangerous to rely upon the results of the EXAFS analysis alone.

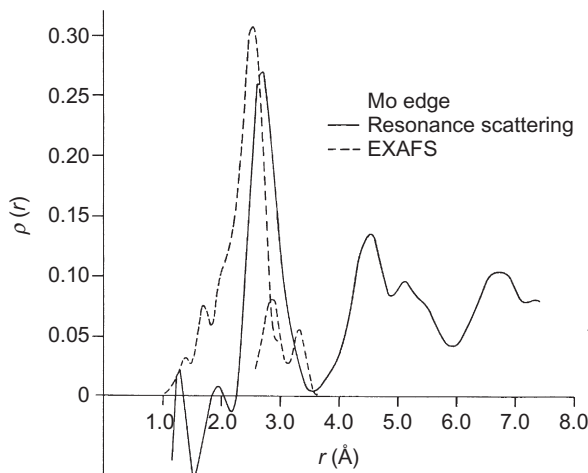


FIGURE A3.3.1 Comparison of the differential PDF of amorphous $\text{Mo}_{50}\text{Ni}_{50}$ determined using EXAFS and anomalous X-ray scattering at Mo and Ni edges (Aur *et al.*, 1983).

APPENDIX 3.4. ANISOTROPIC PDF METHOD

It is recommended to normalize the spherical harmonics functions by

$$\int Y_{\ell}^m(\Omega) Y_{\ell'}^{m'}(\Omega) d\Omega = 4\pi \delta(\ell, \ell') \delta(m, m'), \quad (\text{A3.4.1})$$

where $Y_{\ell}^m(\Omega)$ is the spherical harmonics function, and Ω is the solid angle. Usually, the spherical harmonics are normalized to unity, without 4π in Eq. (A3.4.1). However, we prefer the expression above so that the isotropic structure function, $S_0^0(Q)$, and the isotropic PDF, $g_0^0(r)$, approach unity at large Q or r . The examples of the spherical harmonic functions thus normalized are as follows:

$$\begin{aligned} Y_0^0(\Omega) &= 1, \\ Y_2^0(\Omega) &= \frac{\sqrt{5}}{2} (3 \cos^2 \theta - 1) = \frac{\sqrt{5}}{2} \left(3 \frac{z^2}{r^2} - 1 \right), \\ Y_2^{\pm 1}(\Omega) &= \sqrt{\frac{15}{2}} \sin \theta \cos \theta (\cos \phi \pm i \sin \phi) = \sqrt{\frac{15}{2}} \frac{z(x \pm iy)}{r^2}, \\ Y_2^{\pm 2}(\Omega) &= \sqrt{\frac{15}{8}} \sin^2 \theta (\cos 2\phi \pm i \sin 2\phi) = \sqrt{\frac{15}{8}} \frac{(x \pm iy)^2}{r^2}. \end{aligned} \quad (\text{A3.4.2})$$

Some of the spherical Bessel functions are as follows:

$$\begin{aligned} J_0(z) &= \frac{\sin z}{z}, \\ J_2(z) &= (3 - z^2) \frac{\sin z}{z^3} - \frac{3 \cos z}{z^2}. \end{aligned} \quad (\text{A3.4.3})$$

As in Eq. (1.1) the $\ell=2, m=0$ anisotropic PDF is given by,

$$g_2^0(r) = \frac{\sqrt{5}}{4\pi r^2 \rho_0 N} \sum_{i,j} \frac{1}{2} (3 \cos^2 \theta - 1) \delta(r - r_{ij}). \quad (\text{A3.4.4})$$

Now, when uniform (affine) strain is applied,

$$\mathbf{r}' = (1 + \bar{\epsilon})\mathbf{r}, \quad (\text{A3.4.5})$$

where \mathbf{r} and \mathbf{r}' describe the atomic positions before and after deformation, respectively, and $\bar{\epsilon}$ is the strain tensor, then

$$g(r') = g(r) - \sum_{\alpha, \beta} r \frac{dg(r)}{dr} \frac{r_\alpha r_\beta}{r^2} \epsilon_{\alpha\beta}, \quad (\text{A3.4.6})$$

where α, β refer to the Cartesian coordinate. When uniaxial stress σ_{zz} is applied, the strain is,

$$\bar{\epsilon} = \begin{pmatrix} -v\epsilon_{zz} & 0 & 0 \\ 0 & -v\epsilon_{zz} & 0 \\ 0 & 0 & \epsilon_{zz} \end{pmatrix}, \quad (\text{A3.4.7})$$

where $\epsilon_{zz} = \sigma_{zz}/E$ and E is the Young's modulus and v is the Poisson's ratio, then

$$\begin{aligned} g_0^0(r') &= g_0^0(r) - \frac{1-2v}{3} \epsilon_{zz} r \frac{dg_0^0(r)}{dr}, \\ g_2^0(r') &= -\frac{2(1+v)}{3\sqrt{5}} \epsilon_{zz} r \frac{dg_2^0(r)}{dr}. \end{aligned} \quad (\text{A3.4.8})$$

REFERENCES

- Abeykoon, M., Malliakas, C.D., Juhas Bozin, E.S., Kanatzidis, M.G. & Billinge, S.J.L. (2012) *Zeits. f. Kristallogr.*, **227**, 248.
- Andrievskii, A.I., Nabitovitch, I.D. & Voloshchuk, Y.V. (1960) *Kristallografiya*, **5**, 369 (English transl.: *Sov. Phys. Crystallogr.* **5**, 349 (1960)).
- Aur, S., Kofalt, D., Waseda, Y., Egami, T., Wang, R., Chen, H.S. & Teo, B.K. (1983) *Solid State Commun.*, **48**, 111.
- Bellissent, R. (1982) *Nucl. Instrum. Methods*, **199**, 289.
- Bhathia, A.B. & Thornton, D.E. (1970) *Phys. Rev. B*, **2**, 3004.
- Borisenko, K.B., Chen, Y., Song, S.A., et al. (2009) *Chem. Mater.*, **21**, 5244.

- Cervellino, A., Giannini, C. & Guagliardi, A. (2006) *J. Comp. Chem.*, **27**, 995.
- Clayton, G.T. & LeRoy, H. (1961) *Phys. Rev.*, **121**, 649.
- Cockayne, D.J.H. (2007) *Annu. Rev. Mater. Sci.*, **37**, 159.
- Cockayne, D.J.H. & McKenzie, D.R. (1988) *Acta Crystallogr. A*, **44**, 870.
- Davissou, C. & Germer, L.H. (1927) *Nature*, **119**, 558.
- Debye, P. (1915) *Ann. Phys.*, **46**, 809.
- Dimitrov, D.A., Röder, H. & Bishop, A.R. (2001) *Phys. Rev. B*, **64**, 14303.
- Egami, T. (1990) *Mater. Trans.*, **31**, 163.
- Faber, T.E. & Ziman, J.M. (1965) *Philos. Mag.*, **11**, 153.
- Farrow, C.L. & Billinge, S.J.L. (2009) *Acta Crystallogr. A*, **65**, 232.
- Farrow, C.L., Shaw, M., Kim, H.J., Juhás, P. & Billinge, S.J.L. (2011) *Phys. Rev. B*, **84**, 134105.
- Fessler, R.R., Kaplow, R. & Averbach, B.L. (1966) *Phys. Rev.*, **150**, 34.
- Fuoss, P.H., Eisenberger, P., Warburton, W.K. & Bienenstock, A. (1981) *Phys. Rev. Lett.*, **46**, 1537.
- Gould, R. (1998). Crystallography News, the newsletter of the British Crystallographic Association, No. 67, December 1998. Available online at <http://gordon.cryst.bbk.ac.uk/BCA/CNews/Dec98/strips.html>. Also, reproduced in the ACA newsletter, spring 1999 edition, available online at the home-page of the American Crystallographic Association (<http://www.hwi.buffalo.edu/ACA/>).
- Grimminger, H., Gruninger, H. & Richter, H. (1955) *Naturwissenschaften*, **42**, 256.
- Guinier, A. (1963) *X-ray Diffraction in Crystals, Imperfect Crystals, and Amorphous Bodies*. San Francisco: W.H. Freeman.
- Guinier, A., Fournet, G., Walker, C. & Yudowitch, K. (1955) *Small-Angle Scattering of X-rays*. New York: Wiley & Sons.
- He, Y., Hu, R., Egami, T., Poon, S.J. & Shiflet, G.J. (1993) *Phys. Rev. Lett.*, **70**, 2411.
- Hendus, H. (1942) *Z. Phys.*, **119**, 265.
- Henninger, E.H., Buschert, R.C. & Heaton, L. (1967) *J. Chem. Phys.*, **46**, 586.
- Henshaw, D.G. (1960) *Phys. Rev.*, **119**, 9.
- Kaplow, R., Averbach, B.L. & Strong, S.L. (1964) *J. Phys. Chem. Solids*, **25**, 1195.
- Kaplow, R., Rowe, T.A. & Averbach, B.L. (1968) *Phys. Rev.*, **168**, 1068.
- Keen, D.A. (2001) *J. Appl. Crystallogr.*, **34**, 172.
- Klug, H.P. & Alexander, L.E. (1968) *X-Ray Diffraction Procedures for Polycrystalline and Amorphous Materials*. New York: Wiley.
- Kodama, K., Ikuba, S., Taguchi, T. & Shamoto, S. (2006) *Acta Crystallogr. A*, **62**, 444.
- Koningsberger, D.C., & Prins, R. (Eds.), (1988). *X-Ray Absorption: Principles, Applications, Techniques of EXAFS, SEXAFS and XANES*. New York: Wiley-Interscience.
- Konnert, J.H. & Karle, J. (1973) *Acta Crystallogr. A*, **29**, 702.
- Krebs, H. & Schultze-Gebhardt, F. (1955) *Acta Crystallogr.*, **8**, 412.
- Levashov, V.A., Billinge, S.J.L. & Thorpe, M.F. (2005) *Phys. Rev. B*, **72**, 024111.
- Louca, D. & Egami, T. (1999) *Phys. Rev. B*, **59**, 6193.
- Louca, D., Kwei, G.H., Dabrowski, B. & Bukowski, Z. (1999) *Phys. Rev. B*, **60**, 7558.
- Lovesey, S.W. (1984) *Theory of Neutron Scattering from Condensed Matter*. Oxford: Oxford Science Publications.
- Lytle, F.W., Sayers, D.E. & Stern, E.A. (1975) *Phys. Rev. B*, **11**, 4825.
- Maddox, B. (2002) *Rosalind Franklin: The Dark Lady of DNA*. New York: Harper-Collins.
- Mark, H. & Wierl, R. (1930) *Naturwissenschaften*, **18**, 205.
- Masadeh, A.S., Bozin, E.S., Farrow, C.L., Paglia, G., Juhas, P., Karkamkar, A., Kanatzidis, M.G. & Billinge, S.J.L. (2007) *Phys. Rev. B*, **76**, 115413.
- McCusker, L.B., von Dreele, R.B., Cox, D.E., Louer, D. & Scardi, P. (1999) *J. Appl. Crystallogr.*, **32**, 36.

- Moss, S.C. & Graczyk, J.F. (1969) *Phys. Rev. Lett.*, **23**, 1167.
- Nanao, S., Dmowski, W., Egami, T., Richardson, J.W. & Jorgensen, J.D. (1987) *Phys. Rev. B*, **35**, 435.
- Ocken, H. & Wagner, C.N.J. (1966) *Phys. Rev.*, **149**, 122.
- Peterson, P.F., Bozin, E.S., Proffen, T. & Billinge, S.J.L. (2003) *J. Appl. Crystallogr.*, **36**, 53.
- Petkov, V., Billinge, S.J.L., Heising, J. & Kanatzidis, M.G. (2000a) *J. Am. Chem. Soc.*, **122**, 11571.
- Petkov, V., Billinge, S.J.L., Shastri, S.D. & Himmel, B. (2000b) *Phys. Rev. Lett.*, **85**, 3436.
- Petkov, V., Jeong, I.-K., Mohiuddin-Jacobs, F., Proffen, T. & Billinge, S.J.L. (2000c) *J. Appl. Phys.*, **88**, 665.
- Petri, I., Salmon, P.S. & Fischer, H.E. (2001) *Phys. Rev. Lett.*, **84**, 2413.
- Price, D.L. & Saboungi, M.-L. (1998) S.J.L. Billinge & M.F. Thorpe (Eds.), *Local Structure from Diffraction*. New York: Plenum.
- Proffen, T., DiFrancesco, R.G., Billinge, S.J.L., Brosha, E.L. & Kwei, G.H. (1999) *Phys. Rev. B*, **60**, 9973.
- Qiu, X., Proffen, T., Mitchell, J.F. & Billinge, S.J.L. (2005) *Phys. Rev. Lett.*, **94**, 177203.
- Ruppersberg, H. & Seemann, H.J. (1965) *Z. Naturforsch. Teil A*, **20**, 104.
- Sayre, A. (2000) *Rosalind Franklin and DNA*. New York: W.W. Norton & Company.
- Shannon, C.E. (1949) *Proc. IRE*, **37**, 10.
- Sinha, S.K., Sirota, E.B., Garoff, S. & Stanley, H.B. (1988) *Phys. Rev. B*, **38**, 2297.
- Soper, A.K. (2000) *Chem. Phys.*, **258**, 121.
- Stern, E.A., Sayers, D.E. & Lytle, F.W. (1975) *Phys. Rev. B*, **11**, 4836.
- Suzuki, K. (1987) in *Methods of Experimental Physics*, vol. **23**, Neutron Scattering, Part B. Eds. Price, D.L. & Sköld, K., Academic Press, New York, p. 243.
- Tarasov, L.P. & Warren, B.E. (1936) *J. Chem. Phys.*, **4**, 236.
- Temkin, R.J., Paul, W. & Connell, G.A.N. (1973) *Adv. Phys.*, **22**, 581.
- Thomson, G.P. & Reid, A. (1927) *Nature*, **119**, 890.
- Thorpe, M.F., Levashov, V.A., Lei, M. & Billinge, S.J.L. (2002) J.L. Billinge & M.F. Thorpe (Eds.), *From Semiconductors to Proteins: Beyond the Average Structure* (pp. 105–128). New York: Kluwer/Plenum.
- Toby, B.H. & Egami, T. (1992) *Acta Crystallogr. A*, **48**, 336.
- Treacy, M.M.J. & Borisenko, K.B. (2012) *Science*, **335**, 950.
- Treacy, M.M.J. & Gibson, J.M. (1996) *Acta Crystallogr. A*, **52**, 212.
- Warren, B.E. (1969) *X-Ray Diffraction*. Dover, New York: Addison-Wesley, Reading.
- Warren, B.E. (1990) *X-Ray Diffraction*. New York: Dover.
- Warren, B.E., Krutter, H. & Morningstar, O. (1936) *J. Am. Ceram. Soc.*, **19**, 202.
- Warren, B.E., Averbach, B.L. & Roberts, B.W. (1951) *J. Appl. Phys.*, **22**, 1493.
- Waseda, Y. (1980) *The Structure of Non-Crystalline Solids*. New York: McGraw-Hill.
- Waseda, Y. (1993) J. Suck, B. Watson, P. Chieux, D. Raoux & C. Riekel (Eds.), *Methods in the Determination of Partial Structure Factors of Disordered Matter by Neutron and Anomalous X-Ray Diffraction*. Singapore: World Scientific.
- Watson, J.D. (2001) *The Double Helix: A Personal Account of the Discovery of the Structure of DNA*. New York: Touchstone Books.
- Wu, Y., Dmowski, W., Egami, T. & Chen, M.E. (1987) *J. Appl. Phys.*, **61**, 3219.
- Yan, X. & Egami, T. (1993) *Phys. Rev. B*, **47**, 2362.
- Yan, X., Egami, T., Marinero, E.E., Farrow, R.F.C. & Lee, C.H. (1992) *J. Mater. Res.*, **7**, 1309.
- Zernicke, F. & Prins, J.A. (1927) *Z. Phys.*, **41**, 184.
- Zewail, A.H. (2006) *Annu. Rev. Phys. Chem.*, **57**, 65.